1    Climatology and Interannual Variability of Quasi-Global Intense Precipitation Using

2                                    Satellite Observations

3

4

5              Martina Ricko,[a] Robert F. Adler,[b] and George J. Huffman[c]

6

7

8                                    *Journal of Climate*

9

13

14    _____

15    *Corresponding author*: Martina Ricko, SGT Inc., 7701 Greenbelt Rd., Suite 400,

16    Greenbelt, MD 20770. E-mail: mricko@sgt-inc.com

17

18    [a]SGT Inc., Greenbelt, Maryland

19    [b]Earth System Science Interdisciplinary Center, University of Maryland, College Park,

20        College Park, Maryland

21    [c]NASA Goddard Space Flight Center, Greenbelt, Maryland

22      **Abstract**

23      Climatology and variations of recent mean and intense precipitation over a near global

24      (50°S-50°N) domain on a monthly and annual time scale are analyzed. Data used to

25      derive daily precipitation to examine the effects of spatial and temporal coverage of

26      intense precipitation are the current Tropical Rainfall Measuring Mission (TRMM)

27      Multi-satellite Precipitation Analysis (TMPA) 3B42 Version 7 precipitation product, with

28      high spatial and temporal resolution during 1998-2013. Intense precipitation is defined by

29      several different parameters, such as a $95^{th}$ percentile threshold of daily precipitation, a

30      mean precipitation that exceeds that percentile or a fixed threshold of daily precipitation

31      value (e.g., 25 and 50 mm $day^{-1}$). All parameters are used to identify the main

32      characteristics of spatial and temporal variation of intense precipitation. High correlations

33      between examined parameters are observed, especially between climatological monthly

34      mean precipitation and intense precipitation, both over tropical land and ocean. Among

35      the various parameters examined, the one best characterizing intense rainfall is a fraction

36      of daily precipitation ≥25 mm $day^{-1}$, defined as a ratio between the intense precipitation

37      above used threshold and mean precipitation. Regions that experience an increase in

38      mean precipitation likely experience a similar increase in intense precipitation, especially

39      during the El Niño-Southern Oscillation (ENSO) events. Improved knowledge of this

40      intense precipitation regime and its strong connection to mean precipitation given by the

41      fraction parameter can be used for monitoring of intense rainfall and its intensity on a

42      global to regional scale.

## 1. Introduction

Extreme climatic events frequently occur over areas that experience anomalous precipitation regimes on several time scales. Flooding and landslides are good examples of natural hazard events that are highly connected to excessive precipitation on a daily scale (e.g., Wu et al. 2012; Kirschbaum et al. 2012). On a longer time scale, from months to seasons, anomalous lack of precipitation causes drought events producing substantial impacts on agriculture, ecosystems and society, directly affecting water resources, hydroelectric power, and changes of affected areas. Our concerns are more frequently about those natural events that cause huge economic and human losses on a daily scale. Therefore, promptness, regularity and accuracy in predicting these disastrous events (such as flooding and landslides) need constant focus and further improvement in order to minimize damage from these events.

Numerous studies have investigated the changes in intensity, frequency and trends, with causes and importance of these events. Cavalcanti (2012) showed that large-scale features and synoptic weather systems mainly cause heavy precipitation producing flooding in certain regions, over tropical and extratropical areas. A systematic increase in intensity and frequency of heavy precipitation events in tropical and subtropical regions have been clearly evidenced, and observed changes have been shown to be consistent with most climate model projections (e.g., Allan and Soden 2008; Min et al. 2011; Shiu et al. 2012). Even though precipitation extremes are expected to increase in the future over large parts of the globe as global climate warms (Easterling et al. 2000; Kharin et al. 2007; O'Gorman 2012), with higher moisture content being available to form intense precipitation events and provide additional energy to further intensify such events, we

66  still don't know how strong a relationship between the mean state of precipitation and

67  intense precipitation frequency is on the most recent climate scale.

68      Intensity of precipitation events is projected to increase over areas that experience

69  increases in mean precipitation. A direct link between the mean and intense precipitation

70  (i.e., 95th percentile) has already been confirmed in rain-gauge observations and model

71  predictions both in space and time prior 2000 (e.g., Benestad et al. 2012). However, the

72  increases in intense precipitation derived by different model simulations are shown to be

73  higher than those expected in mean precipitation in most tropical and high-latitude areas

74  (e.g., Trenberth et al. 2003; Held and Soden 2006; Kharin et al. 2007). On the opposite

75  side, there is a tendency for drying of the mid-continental areas during warm periods,

76  resulting in greater risk of droughts in those regions. With current climate change, and

77  especially global warming, Lau et al. (2013) provided evidence that both intense

78  precipitation and drought events may increase, indicating most increases in heavy

79  precipitation over wet regions of the tropical zones around the equator, particularly in the

80  Pacific Ocean and Asian monsoon regions. Similarly, arid land areas outside the tropics

81  and regions with moderate precipitation could become drier (Dai 2011). A clear

82  connection between global mean temperature and both mean and intense precipitation on

83  a large-scale spatial domain and a long time scale (1945-1995) has been found by

84  Benestad (2013), indicating a number of useful climate applications.

85      Lau and Wu (2011) have investigated the climatology and changes in precipitation

86  over tropical oceans, however, using a shorter record of the Tropical Rainfall Measuring

87  Mission (TRMM) data (1998-2009). They showed that intense (95th percentile)

88  precipitation is associated with the Intertropical Convergence Zone (ITCZ), South Pacific

89  Convergence Zone (SPCZ) and summer monsoon regions, and experiences large increase

90  coupled to a reduction in light to moderate rain over warmer ocean regions with

91  increasing sea surface temperature (SST). They also found that intense precipitation

92  events are most sensitive to changes in tropical mean SST, and that increases of 80–90%

93  of the most extreme intense rain (the top 5%) per degree SST rise can be expected. In

94  addition, Liu and Allan (2012) have also investigated precipitation extremes in multi-

95  satellite data, and have confirmed a strong positive response of the tropical ocean

96  precipitation to changes in temperature due to El Niño-Southern Oscillation (ENSO)

97  events. It has also been shown that, even over land, extreme precipitation events are more

98  sensitive to climate variability, such as ENSO, than monthly or seasonal total rainfall, and

99  that the frequency of extreme events experiences a larger and spatially more extensive

100  significant increase than these totals, with reduction of light to moderate rain (Grimm and

101  Tedeschi 2009).

102  In order to develop high-resolution regional climate scenarios for climate change

103  impact studies, including global warming, and to investigate ENSO's natural variability,

104  it is necessary first to analyze longer high-resolution climatic precipitation data sets

105  focusing on intense precipitation on a regional to global scale. Unfortunately, large

106  periods of unavailable and poor quality observational data still limit such analysis,

107  together with low representativeness of *in situ* observations. Most previous studies

108  detecting the increased frequency of intense precipitation events in tropical and

109  subtropical regions have used either *in situ* data over land or long-term monthly satellite

110  precipitation data. However, both types of data do not have sufficient spatial coverage

111  and temporal homogeneity to analyze the intense precipitation events in detail.

112 Furthermore, local changes in precipitation and its extremes are highly variable, and

113 highly dependent upon small shifts in the large-scale atmospheric circulation and regional

114 feedbacks that current climate models still cannot simulate correctly. Consequently,

115 current knowledge of changes in the occurrence of global intense precipitation is still

116 quite limited.

117 In this study, we utilize a 16-year record of daily precipitation derived from a uniform

118 high resolution (3-hr temporal and 0.25° grid spatial) Tropical Rainfall Measuring

119 Mission (TRMM) Multi-satellite Precipitation Analysis (TMPA) Version 7 satellite

120 precipitation data over a near-global domain (50°N-50°S), to analyze climatological

121 intense precipitation over land and ocean during the period 1998-2013. The emphasis

122 here is on the climatology of "intense" precipitation, but we will also give parameters

123 such as mean precipitation, fraction of daily precipitation, and conditional daily

124 precipitation rate, to provide a climatological context. For this study, we consider

125 "extreme" precipitation to be only precipitation amount above the $99^{th}$ percentile

126 threshold, but this parameter is not the focus of this study. Rather, we explore the use of

127 various measures of intense precipitation, including high percentile thresholds (e.g., $95^{th}$

128 percentile), mean precipitation above that percentile, number of days in a month above

129 some daily fixed thresholds (e.g., 25 and 50 mm $day^{-1}$), and mean precipitation above

130 those daily thresholds in a month. Consequently, the parameter that best describes a

131 relationship between the mean precipitation and intense precipitation is analyzed, and can

132 then be easily adopted globally and/or regionally to investigate regions that experience

133 natural hazard events, such as floods and landslides, as has already been done in a

134 preliminary fashion for landslides (Kirschbaum et al. 2012).

135   In addition, we investigate spatial and temporal variations of intense precipitation in

136   relation to its natural variability (i.e., ENSO events), rather than to climate change.

137   Several previous studies (e.g., Curtis et al. 2007; Grimm and Tedeschi 2009; Lau and Wu

138   2011) have already analyzed the ENSO influence on intense precipitation mostly over

139   land and Dai et al. (1997) have found that ENSO is the single largest cause of global

140   intense precipitation over land.

141   The objectives of this study are: (1) to define the best parameter that will help

142   establish the pattern and characteristics of climatology of intense precipitation events, and

143   (2) to understand inter-annual variations of monthly mean and intense precipitation

144   relating them to large-scale climate variability (e.g., ENSO), using recent uniform

145   satellite data over land and ocean over the tropical and sub-tropical domain. The

146   remainder of this paper is organized as follows. Section 2 describes the data products

147   used. Definitions for intense precipitation and analysis procedure are explained in section

148   3. Spatial patterns of intense precipitation climatology are explained in section 4. The

149   results of the intense precipitation characteristics, both over land and ocean, and during

150   El Niño and La Niña periods, are described and examined in section 5. Discussion and

151   conclusions are presented in section 6.

152   **2.  Data**

153   In this study, we utilize the Version 7 TMPA satellite precipitation product (TMPA

154   3B42 V7; Huffman et al. 2007, 2010), which provides near-global coverage (50°N-50°S)

155   at 3-hourly, 0.25° resolution. The TMPA precipitation estimates are a combination of

156   different space-borne sensors, including radar and passive microwave, infrared data, and

157   gauge measurements. Several important changes are included in the TMPA V7 data

158    products: (1) additional satellite data, including the early part of the Microwave Humidity

159    Sounder (MHS) record, the entire operational Special Sensor Microwave Imager/Sounder

160    (SSMIS) record; (2) a new infrared (IR) brightness temperature data set from

161    geosynchronous satellites for the period before the start of the Climate Prediction Center

162    (CPC) 4-km Merged Global IR data set (January 1998–February 2000) with the National

163    Climatic Data Center (NCDC) GridSat-B1 spatial resolution finer than the TMPA 0.25°

164    resolution and full coverage of the TRMM domain; (3) uniformly reprocessed input data

165    from several additional sources: the Advanced Microwave Sounding Unit-B (AMSU-B),

166    MHS, TRMM Combined Instrument (TCI), TRMM Microwave Imager (TMI), the

167    Special Sensor Microwave/Imager (SSM/I), and the Advanced Microwave Scanning

168    Radiometer-Earth Observing System (AMSR-E); and (4) adjustment by the Global

169    Precipitation Climatology Centre (GPCC) monthly surface precipitation gauge analysis

170    (Schneider et al. 2011). An additional retrospective processing for the TMPA V7 data

171    series had to be carried out when processing issues were discovered omitting the AMSU

172    microwave precipitation data during 2000-2010 in the first retrospective processing

173    (Huffman and Bolvin 2012).

174    Several recent studies have addressed the uncertainty of high-resolution global

175    satellite precipitation products, showing their performance depending on the precipitation

176    regime, being more accurate during summer times and at lower latitudes (Arkin et al.

177    2008; Ebert et al. 2007). For daily bias and precipitation frequency, Ebert et al. (2007)

178    showed that the Infra-Red/Passive Microwave merged satellite precipitation estimates are

179    almost as good as those from ground-based radar over the United States. In addition,

180    Sapiano and Arkin (2009) performed an inter-comparison between several high-

181    resolution global satellite products with gauge data, and showed good performance of

182    satellite precipitation data but with relatively high biases (except for gauge-adjusted

183    products over land).

184    Su et al. (2008) evaluated an earlier Version 6 (V6) of the TMPA 3B42 precipitation

185    data set using rain gauge data on various temporal and spatial scales. Good qualitative

186    agreement was found between the TMPA and gauge data in the occurrence of

187    precipitation events, but an overestimation of most high precipitation events on a daily

188    scale over the La Plata basin in South America was observed with noticeable regional

189    variation of the TMPA performance. On a daily scale over the contiguous United States,

190    a study by Tian et al. (2009) showed a comparison of six different high-resolution

191    satellite-based precipitation data sets (including the TMPA 3B42 V6 and TMPA 3B42

192    RT) against the gauge data. Overall, all precipitation data sets showed overestimation of

193    strong precipitation (>40 mm day$^{-1}$) in summer and underestimation in winter, by as

194    much as 50% in either season, and missing a significant amount of light precipitation

195    (<10 mm day$^{-1}$) up to 40%. Consistently missed precipitation in winter was mainly

196    observed over mountainous regions, such as the Rockies, and the northeastern U.S.,

197    confirming a common challenge to all satellite data sets. In addition, Scheel et al. (2011)

198    confirmed that the same TMPA 3B42 V6 estimates in the Central Andes are significantly

199    better on a monthly scale, but overestimation of heavy precipitation still exists.

200    Therefore, we examine here the latest TMPA 3B42 V7 precipitation data set and its

201    performance in the occurrence of heavy rainfall events (i.e., climatological intense

202    precipitation).

203    **3. Methodology and definitions**

204 We compute a daily precipitation data set from 3-hourly TMPA 3B42 V7 for the

205 period of 1998-2013, keeping the original 0.25° spatial resolution. This daily

206 precipitation data set is used to compute monthly statistics over a 16-year climatology of

207 various parameters related to mean and heavy precipitation on a monthly and annual time

208 scale. To set the context of the discussion, we use the total daily precipitation value (R) at

209 each grid point to calculate the mean monthly value of daily precipitation for each month

210 in the year, for the 1998-2013 period ($R_{mean}$, in mm $day^{-1}$). We also compute the

211 conditional precipitation rate for the month (i.e., the mean precipitation rate for days with

212 R >0 mm $day^{-1}$; $R_{cond}$, in mm $day^{-1}$) and the fraction of daily precipitation for days in the

213 month with R >0 mm $day^{-1}$ ($F_0$). These three parameters are related (i.e., $R_{mean}=F_0 \cdot R_{cond}$).

214 For examining intense daily precipitation, we explored a number of statistical

215 parameters to determine monthly values useful for spatial and temporal comparison. Our

216 definitions of these parameters follow closely, but not exactly, those of the Expert Team

217 on Climate Change Detection and Indices (ETCCDI, Karl et al. 1999; Peterson et al.

218 2001). We have specifically examined parameters such as percentiles near the high end of

219 the precipitation distribution, frequency (number of days) above a threshold, and

220 precipitation amounts over certain thresholds. This has been done to attempt to find

221 statistics that would be useful for description of climatology and variations on a monthly

222 scale, and for possible use and links to natural hazards, such as floods and landslides over

223 land, and tropical cyclones and other phenomena over ocean.

224 Since we have a data set with a limited number of years; in terms of percentiles, we

225 have stayed with a relatively conservative value to characterize "intense" daily rainfall

226 (i.e., the 95th percentile). We calculated the 95th percentile of daily precipitation ($R_{95p}$, in

227 mm day$^{-1}$), and the mean precipitation in a month above this daily threshold ($R_{95}$, in mm

228 day$^{-1}$). In addition, we have calculated the number of days in a month with daily

229 precipitation above fixed threshold values (R ≥25, 50 and 75 mm day$^{-1}$; $N_{25}$, $N_{50}$, $N_{75}$),

230 and the intense precipitation above the same daily thresholds ($R_{25}$, $R_{50}$, in mm day$^{-1}$). The

231 fraction of intense precipitation is calculated for all examined thresholds as well ($F_{95}$, $F_{25}$,

232 $F_{50}$), balancing their corresponding intense precipitation amounts ($R_{95}$, $R_{25}$, $R_{50}$) with the

233 mean precipitation (e.g., $F_{95}=R_{95}/R_{mean}$). Results from examining these different statistical

234 parameters allowed us to focus on just a few of them when we moved onto the relations

235 between variables and their inter-annual variations. Table 1 summarizes the definitions

236 and units for all statistical parameters we use to explain climatology of mean and intense

237 precipitation.

238 **4. Climatology of monthly mean precipitation**

239 There are few high quality global or quasi-global climatologies of precipitation that

240 span both land and ocean. The relatively recent TRMM data (1998-present) has resulted

241 in significant new knowledge regarding rainfall system structure and other attributes

242 across the tropics and also a rainfall climatology, the TRMM Composite Climatology

243 (TCC) (Adler et al. 2009; Wang et al. 2014), based on information from both the TRMM

244 Precipitation Radar (PR) and the satellite's passive microwave sensor, the TRMM

245 Microwave Imager (TMI). The Global Precipitation Climatology Project (GPCP)

246 monthly product (Adler et al. 2003; Huffman et al. 2009) is a widely used analysis at 2.5°

247 latitude-longitude resolution covering a time period over 30 years. Even though there

248 exists a GPCP daily product (Huffman et al. 2001), for a similar time span as the TMPA,

249 the TMPA has a higher spatial resolution (0.25°) and is considered of higher quality due

250   to the greater amount of microwave-based rainfall estimates in it. The absolute

251   magnitudes of estimated mean precipitation over ocean are probably best estimated by

252   the GPCP and TCC, which have very similar ocean totals, but with some relatively small

253   regional differences. The TMPA may be overestimating mean values over the ocean

254   somewhat (~8%) due to processing and calibration issues (Huffman and Bolvin 2012).

255   However, this issue does not detract significantly from the search for information on the

256   time and space scales of this study. The mean precipitation values over land in the TMPA

257   are also not impacted by this issue.

258      The annual, January, and July means of daily rainfall ($R_{mean}$) are shown in Fig. 1. The

259   annual climatology map shows very clear features of the Inter-Tropical Convergence

260   Zone (ITCZ) across both the Pacific and Atlantic Oceans, with a not-as-narrow extension

261   through the Maritime Continent into the Indian Ocean. In the Atlantic and Pacific

262   Oceans, the axis of the annual maximum is just north of the equator, while in the Indian

263   Ocean axis falls south of that marker. A northwest-southeast extension of the ITCZ in the

264   South Pacific Ocean, called the South Pacific Convergence Zone (SPCZ), is another

265   feature with the maximum values of mean rainfall. Over tropical land, most striking

266   features with significant rainfall are located over the equatorial African and South

267   American regions. At higher latitudes, two characteristic precipitation bands associated

268   with extensions of ocean currents (the Gulf Stream in the North Atlantic Ocean and

269   Kuroshio in the North Pacific Ocean) are observed along the east coasts of North

270   American and Asian continent, both with significant annual rainfall amounts. The

271   January and July maps show the distinct shift of the seasonal rains with migration of the

272   sun over the tropics, with a larger shift over land than over water describing the

273    monsoons. Enlarged heavy rainfall areas in January are observed in the equatorial

274    Atlantic and the western Pacific, especially over the SPCZ, coastal Southeast Asian

275    region, western extension of the South Equatorial Current in the Southwestern Indian

276    Ocean, and east and north of Madagascar. At mid-latitudes, the rain bands associated

277    with the Gulf Stream and Kuroshio currents are enlarged and extended towards the

278    central and eastern parts of the oceans. Over the land, a shift of maximum rainfall

279    towards the south of the equator in Africa, South America and northern Australia is

280    clearly observed. A coastal region with significant rain is also found in the tropical and

281    subtropical South America, over the northern, southeastern and southern coast of Brazil

282    (including the eastern parts of the Rio de La Plata basin), and over the South Atlantic

283    Ocean along the Brazilian coast. In July, a strong shift of maximum rainfall towards the

284    north of the equator is observed in the ITCZ and SPCZ regions in the Pacific and Atlantic

285    Oceans. Over land, heavy rain regions are found north of the equator in Africa, Central

286    and South America, and near the Asian mountainous regions (i.e., the Tibetan Plateau)

287    where orographic effect enhances the total rainfall amount. In addition, at higher

288    latitudes, northeastern Asian land and coastal regions experience higher rainfall during

289    the Northern Hemisphere summer months. Bands of enhanced rainfall from storm tracks

290    over the Southern Hemisphere mid-latitudes of the Pacific and Atlantic Oceans are

291    observed as well. Overall, we can observe higher maximum values with smaller spatial

292    coverage of rainfall in July than in January.

293    **5.  Climatology of fraction of days with precipitation**

294    Figure 2 displays maps of the fraction of days with rain $>0$ mm day$^{-1}$ ($F_0$). This

295    fraction ($F_0$) multiplied by the conditional precipitation rate ($R_{cond}$, Fig. 3) is equal to the

296    mean precipitation value ($R_{mean}$, Fig. 1), that is, $F_0 = R_{mean}/R_{cond}$, and describes how often

297    it precipitates, irrespective of the amount. The main precipitation areas are clearly

298    evident, as expected, with very high fractions (>0.7) in the annual map along the ITCZ

299    over both ocean and land, with secondary maxima averaging ~0.6 over the middle

300    latitude oceans, especially over the Northern Hemisphere. When examining the maps of

301    monthly climatologies (shown here just January and July, Fig. 2), the fractional days of

302    precipitation ($F_0$) over the higher latitude oceans are now roughly equivalent of those in

303    the tropics, especially during the Northern Hemisphere winter. For example, in January

304    the value of $F_0$ over the Pacific and Atlantic Oceans at about 30°N is the same as the $F_0$

305    values over the deep tropics (between 0.7-0.9). Therefore, at these higher latitude

306    locations, as expected, precipitation is as frequent as in the tropical belt maxima, but the

307    intensity on average is lower.

308        The conditional precipitation rate ($R_{cond}$), or how hard it is precipitating when

309    precipitation is occurring, is a first measure of intensity in this study. As seen in Fig. 3,

310    $R_{cond}$ has a different geographic distribution than the two previous parameters. Even on

311    the annual map, $R_{cond}$ maxima appear in locations where they were absent or muted in the

312    $R_{mean}$ and $F_0$ maps, including eastern China, eastern North America, southeastern South

313    America and other smaller areas over land. In the seasonal maps, during the Northern

314    Hemisphere winter (January) higher values of $R_{cond}$ (>14 mm day$^{-1}$) are observed mostly

315    over the tropical Southern Hemisphere (5°N-25°S), including most of the South

316    American land, northern Australia, Indonesia and parts of southeast African land, and

317    over ocean the SPCZ and the Indian Ocean area. In mid-latitudes, eastern parts of North

318    American land and Euro-Asian land with eastern China experience higher values of $R_{cond}$

(even >16 mm day$^{-1}$). A northward shift of high values is observed during the Southern

Hemisphere winter (July), when land (20°N-0°) experiences extremely high values of

$R_{cond}$ over most of Southeast Asia, including India, Indonesia, Central America, northern

South America and the La Plata basin, and northern tropical Africa; while maximum

values of $R_{cond}$ over ocean are observed in most of the ITCZ and in particular over the

Gulf Stream region. Over the monsoon areas of Asia and Australia, one can easily see the

monsoon associated with intense rainfall events switching back and forth between the

hemispheres, from January to July (Fig. 3b-c). In January, the features over eastern China

and the U.S. are associated with winter cyclone events. Perhaps the most interesting

features are over South America, where a large area of high values exists in January from

the Amazon southward, while in July (local winter) two maxima in $R_{cond}$ exist over the

northern Amazon and the southeastern coast (the La Plata basin). A maximum point

value of the highest conditional mean precipitation rate in the tropical region is observed

to be 44 mm day$^{-1}$ in January over the southern Philippines and 53 mm day$^{-1}$ in July over

the Meghalaya mountains and west coast of India, with 30 mm day$^{-1}$ in the annual mean

observed over the western coast of Colombia (Fig. 3). The month with the lowest

maximum value of $R_{cond}$ is April (35 mm day$^{-1}$ over the northern Arabian Sea), while

February surprisingly reaches the highest maximum point value of 122 mm day$^{-1}$ over

some eastern parts of Ethiopia due to a second rainy season lasting until the end of

February (figures not shown).

## 6. Climatology of intense rainfall

As described in the previous section, many previous studies (e.g., Gu et al. 2007;

Adler et al. 2008; Huffman et al. 2009; Lau and Wu 2011) have been devoted to

342  characterize climatological features of mean precipitation, along with their patterns and

343  variability. Here focus is more on daily intense precipitation events, their means, patterns,

344  anomalies, and variations, using the best currently available consistent high-resolution

345  multi-satellite TMPA precipitation data set. A number of parameters related to intense

346  daily precipitation are examined, keeping in mind the relatively short duration of the data

347  set (16 years, 1998-2013).

348  *6.1. 95$^{th}$ percentile of precipitation*

349  The first set of intense precipitation variables we examine is related to the 95$^{th}$

350  percentile of precipitation. That particular percentile was chosen instead of, for example,

351  the 99$^{th}$ percentile, to give a good measure of intense precipitation events, but also to

352  avoid producing a very noisy field at the higher percentile due to a relatively short data

353  record. One goal of examining these measures of intense precipitation on a daily scale is

354  to understand how they relate to each other, and which ones are the best parameters to

355  focus on, especially in relation to hazardous impacts (e.g., floods and landslides).

356  The distribution of the 95$^{th}$ percentile value ($R_{95p}$) is shown in Fig. 4.  This parameter

357  is defined as a daily precipitation rate threshold (including zero values, in mm day$^{-1}$) in a

358  month at a grid point, below which 95% of the daily rainfall amounts occur, so 5% of all

359  the days have rainfall amounts greater than this value. For example, for months with 30

360  days in a month, the days with precipitation $\geq$95$^{th}$ percentile are 1.5 days, meaning $R_{95p}$

361  contribution is from the heaviest rainfall of 1 or 2 days. The characteristic pattern of $R_{95p}$

362  follows that of $R_{mean}$ and $F_0$ in the annual mean, with the typical features of the

363  atmospheric general circulation over the tropics: the ITCZ, SPCZ, and enhanced rainfall

364  over the Maritime Continent (Southeast Asia), northern tropical Africa, and Central and

365 northern South America; with a strong north-south precipitation gradient. Maximum

366 values observed in $R_{mean}$ are in the range of 10-20 mm day$^{-1}$ (with an absolute maximum

367 of 24 mm day$^{-1}$; Fig. 1a), while $R_{95p}$ gives much higher values (up to 104 mm day$^{-1}$; Fig.

368 4a), as expected.

369 Representative months of two contrasting seasons, January and July, are chosen for

370 analysis of opposite regimes of intense monthly mean precipitation, addressing its

371 seasonal variation (Fig. 4b-c). A north-south migration of the ITCZ is clearly observed

372 where maximum precipitation regions reside, especially over land. A strong maximum of

373 $R_{95p}$ (up to 47 mm day$^{-1}$) during July is also observed over the eastern parts of the Rio de

374 la Plata basin, located in south-central South America (La Plata hereafter), with a

375 seasonal shift northwards in January (Fig. 4b-c). A maximum value of mean precipitation

376 over the tropics is 27 mm day$^{-1}$ in January and 43 mm day$^{-1}$ in July (Fig. 1b-c), while $R_{95p}$

377 has a maximum value of 142 mm day$^{-1}$ in January and 190 mm day$^{-1}$ in July (Fig. 4b-c),

378 clearly indicating the wettest period in the tropics during boreal summer. The month with

379 the lowest maximum value of $R_{mean}$ over the tropics is April, with a maximum of 22 mm

380 day$^{-1}$, while $R_{95p}$ reaches maximum of 102 mm day$^{-1}$ (figures not shown).

381 The only areas that are wetter during the boreal winter season than the rest of the year

382 are the westerly storm tracks regions over the Pacific and Atlantic Oceans in mid-

383 latitudes, with the maximum $R_{mean}$ of 8-11 mm day$^{-1}$ (Fig. 1b) and the maximum $R_{95p}$ of

384 30-50 mm day$^{-1}$ (Fig. 4b). Despite the fact that seasonal variability of precipitation is

385 more pronounced outside of the tropics, where rainy seasons differ much more

386 regionally, we focus on the intense precipitation variability more in the tropical and less

387 in the extra-tropical regions due to the data availability and quality in this region.

388    Even though we are looking at only 16 years of precipitation data, there are some

389    significant differentiating spatial features between mean and intense precipitation that are

390    worth mentioning. In comparison, regions with high intense precipitation (i.e., $R_{95p}$) are

391    significantly larger in area than those characterized by mean precipitation ($R_{mean}$) over

392    most of the studied quasi-global domain, except over drier land and ocean regions such as

393    Northern Africa, South Asia and Australia during dry seasons; and west coast of South

394    America, Central America, and parts of North America, where locally the 95th percentile

395    amount is very close to the mean precipitation value due to its small values and

396    insignificant seasonal variations in precipitation. The 95th percentile precipitation varies

397    greatly between months and seasons in some locations. For example, this seasonal

398    variability is most apparent at sites in the north of Australia, where during the wet season

399    (December-May) some locations experience 95th percentile rainfall higher than 50 mm

400    day$^{-1}$, while during the drier months (June-November) the same locations show tiny

401    rainfall values. A rough factor of 5-6 between the mean precipitation ($R_{mean}$) and $R_{95p}$,

402    and a factor of 3-4 between the mean rain rate ($R_{cond}$) and $R_{95p}$ is observed in the annual

403    mean over the tropics that experiences most of the rainfall (figures not shown).

404    Therefore, we investigate other similar statistical parameters that can better characterize

405    the intense precipitation regime in recent years.

406    *6.2. Mean and fraction of precipitation above the 95th percentile*

407    While the $R_{95p}$ parameter gives some insight into the distribution of heavy

408    precipitation, other additional parameters need to be examined to offer more detailed

409    explanations and relations of parameters that accent the intense precipitation. One such

410    parameter that emphasizes the amount of precipitation occurring during intense events is

411   the monthly mean precipitation with rainfall $\geq 95^{th}$ percentile ($R_{95}$, in mm day$^{-1}$), defined

412   as the total amount of precipitation $\geq R_{95p}$ in a month divided by the number of days in

413   that month (see Table 1). The spatial patterns of $R_{95}$ (Fig. 5) and $R_{mean}$ (Fig. 1) are similar

414   over most regions, as expected, although the $R_{95}$ patterns emphasize somewhat the areas

415   with heavy rainfall. However, the fraction of rainfall that exceeds the $95^{th}$ percentile to

416   the mean rainfall ($F_{95}=R_{95}/R_{mean}$, figure not shown) tends to vary inversely to $R_{95}$. Over

417   areas of higher mean rain rates, the ratio $F_{95}$ is 0.2 to 0.3, indicating that 20-30% of

418   monthly rain occurs at daily rates above or equal to the $R_{95p}$ threshold. On the other hand,

419   in the areas with light rainfall, the ratio $F_{95}$ is high (~0.8-1), because the $R_{95p}$ threshold is

420   very close to the mean rain rate with only one or two rain events in the month that

421   account for all of the rain. Therefore, while both the $R_{95}$ and $F_{95}$ parameters are of

422   interest, they are of limited value in discerning spatial and temporal variations of heavy

423   rainfall.

424   *6.3. Mean and fraction of precipitation above fixed thresholds*

425   Floods and landslides are usually associated with an absolute amount of precipitation

426   physically related to overflowing banks and/or moving soil from a slope - not from

427   exceeding a local percentile threshold. So, another approach to investigate the intense

428   precipitation characteristics is to examine intense precipitation parameters by evaluating

429   the fraction of days in a month with precipitation that exceeds fixed threshold values

430   (e.g., 25, 50 and 75 mm day$^{-1}$; $F_{25}$, $F_{50}$ and $F_{75}$). The maximum value observed in the

431   annual mean number of days with intense precipitation defined by the $95^{th}$ percentile is

432   1.6 days/month (5%). Consequently, extremes based on the respective $95^{th}$ percentile

433   (Fig. 4) show somewhat different spatial patterns than what is observed on maps of

434  fraction of days in a month with precipitation defined by any fixed thresholds over the

435  same locations and at the same time, due to a different selection of precipitation intensity

436  values.

437  The specific total daily precipitation threshold commonly used for determining

438  intense precipitation varies among regions and countries. A few examples of different

439  fixed thresholds, used by the national weather services or previous studies (e.g.,

440  Easterling et al. 2000; Gustafsson et al. 2010), give values of 20-40 mm day$^{-1}$ for Norway

441  and Sweden, 20 mm day$^{-1}$ for most of Russia and southern Canada, 50.8 mm day$^{-1}$ for the

442  United States, Brazil, South Australia, northeastern China, Equatorial East Africa and

443  South Africa, and 100 mm day$^{-1}$ for Japan and southeastern China.

444  In this study, characteristic spatial signatures of $F_{25}$, $F_{50}$ and $F_{75}$ for January and July

445  are compared to those observed in the mean precipitation ($R_{mean}$). The results show fairly

446  similar spatial patterns between these parameters, with a lower fraction of intense

447  precipitation by half going from 25 to 50 mm day$^{-1}$. The spatial distribution of monthly

448  mean frequency of intense rainfall (in days) suggest that local extremes in the tropics

449  occur mostly from June to August, with maximum values of 17, 10 and 6 days for the

450  three thresholds of 25, 50 and 75 mm day$^{-1}$ ($N_{25}$, $N_{50}$, and $N_{75}$, figures not shown).

451  August noticeably receives the highest frequency of extremes for 25 and 50 mm day$^{-1}$

452  thresholds, while June receives it for 75 mm day$^{-1}$ threshold. The period from September

453  to May is relatively quieter with respect to high season extremes, with maximum point

454  values of 14, 8 and 4 days observed for the three fixed thresholds. A strong seasonality of

455  intense precipitation frequency and its temporal dependence on the mean precipitation is

456    observed with clustering of extremes over the regions that experience the highest values

457    of mean precipitation.

458         Maps of climatological daily precipitation greater than several different thresholds

459    (i.e., above 0, 25 and 50 mm day$^{-1}$, and 95$^{th}$ percentile; $R_{mean}$, $R_{25}$, $R_{50}$, and $R_{95}$) show

460    their highest amounts over similar geographic areas both over land and ocean in the

461    annual and monthly climatologies. Fraction of days parameters with intense rainfall ≥25

462    and 50 mm day$^{-1}$ ($F_{25}$ and $F_{50}$) follow this similar spatial pattern that is observed in $R_{mean}$

463    as well.

464         Another measure of intense rainfall is the monthly mean rainfall ≥25 and 50 mm day$^{-1}$

465    ($R_{25}$ and $R_{50}$, Fig. 6). The features here correspond well with spatial features previously

466    observed for the typical mean rainfall, but are weaker in intensity than for $R_{mean}$ and

467    stronger than for $R_{95}$. Both $R_{25}$ and $R_{50}$ exhibit similar patterns, but a higher threshold

468    value of 50 mm day$^{-1}$ filters out some of the extended features by depicting only areas

469    with higher amounts of rainfall. $R_{25}$ can reach a maximum point value up to 24 mm day$^{-1}$

470    in January and 38 mm day$^{-1}$ in July, with 20 mm day$^{-1}$ in annual mean, but high values

471    have a range of 5-10 mm day$^{-1}$ (Fig. 6a-c). Similarly, a maximum point value of $R_{50}$ can

472    reach up to 20 mm day$^{-1}$ in January and 34 mm day$^{-1}$ in July, with 15 mm day$^{-1}$ in annual

473    mean map (Fig. 6d-f), having high values between 3-8 mm day$^{-1}$. In comparison, $R_{mean}$

474    over the tropics has a maximum point value up to 27 mm day$^{-1}$ in January and 43 mm

475    day$^{-1}$ in July, with a maximum value of annual mean up to 24 mm day$^{-1}$ (Fig. 1). From

476    monthly climatologies, April consistently exhibits the lowest amounts of $R_{25}$ and $R_{50}$,

477    similarly as observed in $R_{mean}$, $R_{cond}$, and $R_{95}$.

478    Based on the preceding analysis, $R_{25}$ (Fig. 6a-c) is chosen to be a key parameter for

479    intense precipitation (hereafter intense precipitation). Therefore, we examine the intense

480    rainfall parameter in relation to the mean rainfall. The ratio $F_{25}$, defined as $R_{25}/R_{mean}$,

481    gives the fraction of rain that falls above 25 mm in a day. Over a period of time (e.g., a

482    month), it is designed to emphasize areas and times when much of the rain falls during

483    days with intense rainfall. $F_{25}$ (Fig. 7) shows some clear differences between two

484    parameters ($R_{25}$ and $R_{mean}$), giving some characteristic spatial features that are not

485    observed in previously defined parameters, and some similar features that are wider in

486    coverage with a weaker gradient than what is observed for $R_{cond}$ (a first measure of the

487    intensity examined in this study).

488    High intensity parameters are distributed both over land and ocean and higher in the

489    tropical latitudes. However, intense rainfall events with rain $\geq 25$ mm day$^{-1}$ are observed

490    somewhat more over ocean areas (Fig. 7) in comparison to the highest values of $R_{cond}$ that

491    are located more over land (Fig. 3). On the annual map (Fig. 7a), maxima in $F_{25}$ appear in

492    locations similar to those observed in $R_{cond}$, but also including more intensified locations

493    with wider spatial coverage over ocean and along the coasts, such as: east coast of

494    Australia, most of the mid-latitudes areas of both the Atlantic and Pacific Oceans, and

495    slightly wider equatorial Atlantic and Pacific Ocean regions (i.e., the ITCZ). A rough

496    factor of 0.65-0.75 for $F_{25}$ is observed in the annual mean over the tropical region with

497    the highest rainfall amounts.

498    Strong seasonal variations in this intense rainfall measure are very similar to those

499    observed in $R_{cond}$. However, higher values of $F_{25}$ (>0.6) are also observed mostly over the

500    extended tropical and mid-latitudes Southern Hemisphere ocean (7°N-35°S). Over land,

501 the highest values confirm intense events over Southeast Asian areas, related to the strong

502 monsoon phenomenon constantly switching between the Northern and Southern

503 Hemisphere. Similar features and high values over eastern China and the eastern U.S. are

504 associated with strong winter tropical cyclones in January (Fig. 7b). In addition, the most

505 significant features with high values in the Southern Hemisphere are located over a large

506 area of South America in January, while in July (austral winter, Fig. 7c) there are only

507 two maxima in intense rainfall, over the northern Amazonia and the La Plata basin. As

508 higher rainfall amounts tend to occur over previously mentioned moist regions, lower

509 rainfall tends to occur over the dryer regions with more intense convection (e.g., Sahel

510 and eastern Congo in Africa, and Argentina in South America).

511     Features in the monthly maps are consistently located over the areas where tropical

512 cyclones are most common (e.g., east of the Philippines, most of the Indian Ocean, and

513 the northern Gulf of Mexico) and over the La Plata basin, but also over the mountainous

514 regions with strong topographic lifting, where moderate and higher rainfall events last

515 longer. During Northern Hemisphere colder seasons (September-February), higher values

516 and wider spatial features of $F_{25}$ are located over most of the northern Atlantic and

517 Pacific Oceans. During November-March, most observed maxima are located over the

518 wider SPCZ, and a persistently occurring feature across the La Plata basin and over

519 coastal waters in the southern Atlantic Ocean. Another set of maxima is located over the

520 persistent ITCZ and the east coast of Asia in the North Pacific Ocean during Northern

521 Hemisphere warm months (May-October). As observed, the ratio gives very strong

522 seasonal variations over most of the tropical regions. However, a quasi-global mean has a

523 typical value of only 0.34 during winter months (December, January and February) and

524 0.30 during summer months (July and August).

525 Statistical analysis of $R_{25}$, $R_{50}$, and $R_{mean}$ during a 16-year climatological period

526 shows that intense rainfall is highly correlated with $R_{mean}$, with a correlation coefficient

527 (r) of 0.96 for $R_{25}$ and 0.87 for $R_{50}$ (significant at the 95% confidence level) on a monthly

528 time scale over the full domain examined. This highly correlated relationship between the

529 mean and intense precipitation parameters, and their spatial distribution, both over land

530 and ocean during the same time period, is confirmed in other data sets as well (e.g., over

531 the global domain in daily GPCP v1.2, and over the U.S. in daily National Oceanic and

532 Atmospheric Administration [NOAA] Climate Prediction Center [CPC] Unified Data,

533 results not shown here).

534 Fig. 8 shows distributions and correlations between mean precipitation and intense

535 precipitation (over ocean and land separately) using $R_{25}$ and $R_{50}$ as the parameters for the

536 intense component. Slightly lower correlations between intense and mean rainfall

537 parameters are observed when investigating land versus ocean amounts, for both fixed

538 threshold values (Fig. 8). The intense precipitation with the 50 mm day$^{-1}$ fixed threshold

539 gives somewhat lower correlations (r=0.82 for land and 0.89 for ocean) and higher root-

540 mean-square (RMS) differences (3.08 mm day$^{-1}$ for land and 3.00 mm day$^{-1}$ for ocean)

541 than what is observed for the 25 mm day$^{-1}$ threshold (r=0.95 for land and 0.97 for ocean)

542 with lower RMS differences (2.00 mm day$^{-1}$ for land and 1.91 mm day$^{-1}$).

543 Figure 6 shows very characteristic spatial distributions over land and ocean, for both

544 $R_{25}$ and $R_{50}$. The distribution of monthly climatology of $R_{mean}$ against $R_{25}$ (Fig. 8a-b), and

545 against $R_{50}$ (Fig. 8c-d), is presented in such a way that all data values are divided into

546    bins in ascending order, including all grid points over the examined domain. Scatter plots

547    of intense precipitation against mean precipitation show a wider shape at the bottom of

548    the distribution and narrower but with a larger spread at the higher end of precipitation

549    values. There is no significant difference between land and ocean, except for a slightly

550    narrower distribution over ocean (Fig. 8a-b). We observe that the distribution becomes

551    slightly wider in shape with a lower slope of the median fit for a higher threshold chosen

552    ($R_{50}$, Fig. 8c-d).

553    A strong relationship between mean and intense precipitation is well defined by

554    fitting a median line over their spatial distribution. For the 25 mm day$^{-1}$ threshold (Fig.

555    8a-b), a median fit is linear but with two different slopes: for smaller rainfall values

556    between 0-13 mm day$^{-1}$ of $R_{mean}$, a slope for $R_{25}$ is $R_{25}=0.65 \cdot R_{mean}$; and between 13-35

557    mm day$^{-1}$ of $R_{mean}$, the slope increases to $R_{25}=1 \cdot R_{mean}$, both over land and ocean. In

558    comparison, the 50 mm day$^{-1}$ threshold (Fig. 8c-d) gives results similar to the 25 mm day$^{-}$

559    $^{1}$ threshold for higher values (between 13-35 mm day$^{-1}$ of $R_{mean}$, a slope for $R_{50}$ equally

560    increases as in $R_{25}$, i.e., $R_{50}=1 \cdot R_{mean}$), but a decreased slope for the lower values (between

561    0-13 mm day$^{-1}$ of $R_{mean}$, the slope for $R_{50}$ decreases almost double with respect to $R_{25}$,

562    $R_{50}=0.30 \cdot R_{mean}$). Above 20 mm day$^{-1}$ of $R_{mean}$, there are a very few grid points per bin

563    observed ($\leq$10 grids). However, up to that precipitation value we can well define the

564    median fit, which is consistent for the higher precipitation values as well. This result

565    offers a great method to estimate the intense precipitation ($R_{25}$ or $R_{50}$) knowing a true

566    value of the mean precipitation ($R_{mean}$), and vice versa, on a local and global scale.

567    Overall, the observed high correlation values and a strong positive linear relationship

568    between intense precipitation and mean precipitation regimes, in terms of mean or total

569     accumulated amounts on a daily scale, build confidence in defining constant slopes

570     between them. This well-defined relationship and the ratio between two analyzed

571     parameters ($R_{mean}$ and $R_{25}$) may therefore significantly help analyze current and past

572     intensity of rainfall amounts.

573     **7. Interannual variability of intense rainfall**

574     Numerous studies have shown that increase or reduction in mean precipitation are

575     likely to be associated with different phases of natural variability. For instance, recent

576     observations indicate that interannual climatic variability of mean precipitation is

577     strongly related to ENSO over many regions, and that a pronounced increase in intense

578     rainfall events is associated with warm or cold ENSO phases over many regions (e.g.,

579     IPCC 2007; Curtis et al. 2007; Grimm and Tedeschi 2009; Lau and Wu 2011).

580     Interdecadal modes of climate variability also produce changes in mean precipitation, as

581     well as in the frequency of extreme events (e.g., Grimm and Saboia 2015; Grimm et al.

582     2016). In order to focus on interannual variability of intense rainfall, we investigate both

583     El Niño and La Niña's influence on mean and intense precipitation.

584     There are just a few strong recent ENSO events observed during the 16-year period of

585     this study (e.g., El Niños in 1998, 2002-03, 2009-10, and La Niñas in 1998-99, 1999-

586     2000, 2007-08, 2010-11, 2011-12). The strength of ENSO is typically defined by using

587     the Niño3.4 monthly anomaly index of sea surface temperature. The Niño3.4 index over

588     the Niño3.4 region (5°N-5°S, 160°E-150°W) used here is obtained from NOAA CPC. El

589     Niño and La Niña periods are defined by choosing El Niño/La Niña months classified as

590     either the top third or bottom third of ranked monthly values of Niño3.4 index anomalies

591     during the available TMPA precipitation data record (1998-2013). Monthly Niño3.4

592    index values considered are then >0.14°C and <-0.62°C. Corresponding monthly values

593    of the TMPA 3B42 V7 precipitation anomalies of mean precipitation (e.g., $R_{mean}$) and

594    intense precipitation (e.g., $R_{25}$ and $R_{50}$) are derived and analyzed for El Niño, La Niña

595    and neutral periods.

596    The strongest ENSO signal is observed over the Pacific and Indian Oceans; however,

597    ENSO also influences many other regions over the globe. Maps of seasonal mean

598    precipitation anomalies ($R_{mean}$) during El Niño period show: a strong precipitation

599    increase over the equatorial Pacific and Indian Oceans, the ITCZ and SPCZ tropical

600    regions, and a slight increase over the Southeast U.S. and the La Plata basin in South

601    America; and a decrease over the Maritime Continent, Amazonia, and the equatorial

602    Atlantic Ocean (Fig. 9a-d). During La Niña, a dipole regime observed in seasonal mean

603    precipitation anomalies is nearly opposite, as expected (Fig. 9e-h). The same persistent

604    regime is also observed in anomalies of mean and intense precipitation ($R_{mean}$, $R_{25}$, and

605    $R_{50}$) during both El Niño and La Niña periods (figures not shown). Figure 9 confirms the

606    strongest ENSO signal and the largest spatial coverage of rainfall amounts during

607    December-January-February (DJF) season, and the weakest signal with the smallest

608    spatial coverage during June-July-August (JJA) season, both for El Niño and La Niña

609    periods, respectively.

610    In a similar way to the monthly analysis of intense rainfall, we investigate a

611    relationship between anomalies of mean precipitation ($R_{mean}$) and intense precipitation

612    (e.g., $R_{25}$) for El Niño, La Niña, and neutral months. Figure 10 shows a set of scatter plots

613    between $R_{mean}$ and $R_{25}$ anomalies during El Niño, La Niña, and neutral periods, over

614    tropical land and ocean. The most pronounced variations in mean precipitation anomalies

615 and the highest maximums in intense precipitation anomalies are observed in the tropics.

616 Therefore, we investigate this strong positive relationship between two parameters for the

617 narrower tropical region (23.5°N-23.5°S). Mean and intense precipitation anomalies in

618 the scatter plots show slightly different characteristics during El Niño versus La Niña

619 periods, with a shift towards more positive versus negative anomalies (red/yellow colors

620 in Fig. 10). With a higher number of grid points (such as over ocean), a tail of the

621 observed linear distribution is longer, both in positive and negative anomalies. Similarly,

622 as expected, a shorter extension of the distribution is observed over land, confirming the

623 highest intense rainfall amounts mostly over the tropical oceans.

624 The results also give consistently higher amounts of positive heavy rainfall anomalies

625 during La Niña period over tropical land and especially during El Niño period over

626 tropical ocean (up to 4 mm day$^{-1}$), observed as an extension of the slightly wider

627 distribution with a larger number of grid points (Fig. 10b,d). In contrast, higher amounts

628 of negative heavy rainfall anomalies are observed during El Niño over land (up to -3.5

629 mm day$^{-1}$) and during La Niña over ocean (up to -4.3 mm day$^{-1}$; Fig. 10a,e). This is all

630 due to placement of land (e.g., South America) in relation to the precipitation variations.

631 The distribution of intense and mean precipitation anomalies for neutral period gives

632 significantly lower rainfall amounts (in a range of ±2 mm day$^{-1}$), with more uniform and

633 symmetrical shape, both over land and ocean. Higher correlations between $R_{mean}$ and $R_{25}$

634 anomalies are observed during El Niño and La Niña periods (r=0.92 for land and r=0.97-

635 0.98 for ocean) versus neutral periods (0.88 for land and 0.94 for ocean). Slightly higher

636 correlations observed over ocean in individual El Niño/La Niña period are probably due

637 to more uniform rainfall data over ocean than over land. A slope of the positive linear

median fit in the distributions of $R_{mean}$-$R_{25}$ anomalies is very similar and consistent for El

Niño and La Niña periods, and slightly higher over land than over ocean ($R_{25}$=0.75·$R_{mean}$

for land and $R_{25}$=0.65·$R_{mean}$ for ocean, Fig. 10a-b,d-e). As noted above, neutral periods

experience much lower change in mean and intense rainfall amounts, but a higher slope

of the linear median fit ($R_{25}$=0.90·$R_{mean}$ for land and $R_{25}$=0.85·$R_{mean}$ for ocean, Fig.

10c,f).

Results similar to those for $R_{25}$ are observed for the $R_{50}$ distribution over the tropics

as well (figure not shown). However, with the higher daily threshold of 50 mm day$^{-1}$,

overall change in $R_{50}$ is even lower than the observed change in $R_{mean}$, with a decreased

slope of the linear median fit in the distribution of rainfall anomalies (a change factor of

0.40-0.50 during El Niño/La Niña period and 0.65-0.70 during neutral period). The $R_{mean}$-

$R_{50}$ distribution gives a wider shape of observed anomalies and slightly lowers

correlations both over land and ocean (0.88-0.98 for $R_{25}$ vs. 0.70-0.88 for $R_{50}$).

**8. Regions with intense rainfall strongly related to ENSO**

A few interesting regions located in areas with the observed peaks in mean and

intense precipitation are chosen for a more detailed analysis of interannual variability of

intense rainfall. The first region is defined over the West Pacific Ocean, as a 5°x5° grid

box (6°S-1°S, 177°E-182°E), over which an average of $R_{mean}$, $R_{25}$ and $R_{50}$ is computed

(Fig. 11). Corresponding time series are analyzed then over the highest amounts of

rainfall, showing the overall variability of intense precipitation ($R_{25}$ and $R_{50}$), following

closely the mean rainfall variation of $R_{mean}$. As expected, high correlations between mean

and intense precipitation anomalies (r=0.99 for $R_{25}$ and 0.95 for $R_{50}$) are observed over

the West Pacific Ocean region (Fig. 11a).

661        The same parameters are also analyzed in relation to the Niño3.4 index. A scatter plot

662    of mean and intense precipitation anomalies with respect to the Niño3.4 index anomalies

663    shows a strong positive linear relationship (Fig. 11b). High correlations of 0.66 for $R_{25}$

664    and 0.61 for $R_{50}$ (both significant at the 95% confidence level) between the Niño3.4 index

665    and intense precipitation anomalies are observed over the West Pacific Ocean region.

666    $R_{mean}$ gives slightly higher correlation of 0.70 with the Nino3.4 index.

667        The West Pacific region is then compared with a 5°x5° region over the Philippines

668    (10°N-15°N, 122°E-127°E) that includes both land and ocean areas, to address main

669    differences between these two regions experiencing the opposite extreme sign in $R_{mean}$,

670    $R_{25}$ and $R_{50}$ anomalies (Fig. 12). The scatter plots of mean and intense precipitation

671    anomalies show strong positive values during El Niño period (red color values in Fig.

672    12a) and strong negative values during La Niña period (blue color values in Fig. 12a)

673    over the West Pacific Ocean region, and the opposite dipole regime with strong positive

674    values during La Niña and strong negative values during El Niño period over the

675    Philippines region (Fig. 12b). During neutral period, anomalies are distributed around a

676    center of the scatter plots. Two contrasting regions give high correlations between mean

677    and intense precipitation anomalies (0.99 for $R_{25}$ and 0.95 for $R_{50}$ over the Pacific region,

678    and 0.98 for $R_{25}$ and 0.94 for $R_{50}$ over the Philippines) and significantly small RMS

679    differences (1.15 mm day$^{-1}$ for $R_{25}$ and 2.23 mm day$^{-1}$ for $R_{50}$ over the Pacific region, and

680    0.72 mm day$^{-1}$ for $R_{25}$ and 1.43 mm day$^{-1}$ for $R_{50}$ over the Philippines).

681        Another pair of smaller secondary peaks in $R_{mean}$, $R_{25}$ and $R_{50}$ anomalies is observed

682    over the continental South America in the La Plata basin (33°S-28°S, 299°E-304°E) and

683    in central Amazonia (5°S-0°, 301°E-306°E). Both regions over the South American land

684     experience strong ENSO signal, but with somewhat weaker precipitation anomalies and a

685     lower $R_{25}/R_{mean}$ ratio than observed in the Pacific/Philippines regions during El Niño/La

686     Niña period. All regions show consistently high significant correlations ranging between

687     0.95-0.99 for $R_{25}$ and 0.81-0.96 for $R_{50}$, with a strong positive linear fit. However, the

688     Pacific/Philippines distributions show higher RMS differences of 0.72-1.15 mm day$^{-1}$ for

689     $R_{25}$ and 1.43-2.23 mm day$^{-1}$ for $R_{50}$ versus South American 0.36-0.71 mm day$^{-1}$ for $R_{25}$

690     and 0.84-1.33 mm day$^{-1}$ for $R_{50}$ (Fig. 12), and this is due to higher rainfall variability over

691     ocean. In addition, El Niño/La Niña identified values over the South American land are

692     not separated in the way they are over the West Pacific/Philippines regions and somewhat

693     in the La Plata basin (distributed only as positive or negative anomalies during El Niño or

694     La Niña, seen in Fig. 12c-d vs. 12a-b), indicating that other factors, besides ENSO, must

695     play a role there. In the La Plata basin, besides mid-latitude effects, there are also other

696     influences from the Pacific and Atlantic Oceans, which play an even more significant role

697     in the Amazon region. They can be similar or opposite to the ENSO influence, enhancing

698     or weakening the resulting effect on both inter-annual and inter-decadal time scales

699     (Grimm 2011; Grimm and Saboia 2015).

700     **9. Discussion and conclusions**

701     Satellite-based estimation of precipitation, specifically the TRMM-based TMPA

702     3B42 V7 analysis has allowed us to examine climatology and variations of recent intense

703     daily precipitation during 1998-2013. This study analyzes different parameters

704     representing mean and intense precipitation, their relationships and variability,

705     contributing to our understanding of the precipitation behavior at climate scale. The

706     relatively short 16-year data record used here limits our examination of extreme daily

707  precipitation, but allows for a careful study of intense daily precipitation, including its

708  climatology and variations that should be related to events such as floods and landslides.

709  This capability is due to the TMPA's relatively high quality, i.e., mostly microwave-

710  based, high resolution (3-hr, 0.25° lat./lon.), continual calibration, continuity, and

711  uniformity over a near-global domain (50°N-50°S).

712     Climatologies of mean rainfall, conditional mean rainfall and fraction of rainfall days

713  are examined and compared, and begin to reveal areas and times where and when heavier

714  rainfall is more frequent. We tested several commonly used parameters to define intense

715  precipitation, such as: mean monthly 95$^{th}$ percentile of daily precipitation, mean and

716  fraction of precipitation that exceeds the 95$^{th}$ percentile, fraction of intense precipitation

717  above fixed daily thresholds of 25 and 50 mm day$^{-1}$, and mean rainfall above same fixed

718  thresholds, to infer which parameter best characterizes the heavy rainfall regime. Spatial

719  patterns and features of various mean and intense precipitation parameters compare well

720  to each other, with some differences over land and ocean. The overall results show a very

721  strong relationship between mean and intense precipitation. Specifically, consistently

722  high significant correlations with a strong positive linear relationship are observed

723  between two interesting parameters: the monthly mean precipitation (mean precipitation

724  $\geq 0$ mm day$^{-1}$, $R_{mean}$) and intense precipitation (mean precipitation $\geq 25$ mm day$^{-1}$, $R_{25}$).

725     Among the various examined parameters, the one best characterizing the intense

726  rainfall is observed to be a ratio between intense precipitation and mean precipitation

727  ($R_{25}/R_{mean}$). This ratio is considered to be a good measure of rainfall intensity. The results

728  show high significant correlations and a strong positive linear relationship between these

729  two parameters ($R_{25}$ and $R_{mean}$), explaining the contribution of intense rainfall to total

730    rainfall. We consider this analysis to be a first attempt of this kind to determine the best

731    measure for intense rainfall.

732        From analysis of interannual variability of intense precipitation, we confirm a strong

733    positive linear relationship and consistently high correlations between mean and intense

734    precipitation anomalies, especially during El Niño and La Niña periods. The results also

735    confirm that El Niño and La Niña events with their effects equally contribute to the

736    observed connection between mean and intense precipitation, with no significant

737    difference between land and ocean. In general, most of the intense rainfall events are

738    observed over tropical ocean. However, the results show that intense rainfall events are

739    stronger and more frequent during La Niña periods over tropical land and during El Niño

740    periods over tropical ocean. Overall, the observed change in intense rainfall anomalies is

741    lower than the one observed in mean rainfall anomalies during El Niño/La Niña period,

742    and it decreases with a higher fixed threshold (a factor of 0.65-0.75 for $R_{25}$ and 0.40-0.50

743    for $R_{50}$).

744        Intense rainfall is the major factor of causing floods and landslides worldwide,

745    especially in recent years. Therefore, improved knowledge of the intense precipitation

746    regime and its strong connection to the mean precipitation on a global to regional scale

747    can offer more consistent current and near-future estimates of heavy rainfall, providing

748    help in preventing damages caused by extreme events (i.e., floods, flash floods, and

749    landslides). Future research should focus on the analysis of intense precipitation and

750    flood events, together with economic and social systems, including additional factors

751    such as population, critical infrastructures, and financial indices of cost that help estimate

752    the potential risks and impacts of extreme and heavy rainfall events. Providing accurate

753    estimates of future intense precipitation events due to climate change, global warming,

754    and/or natural climate variability (i.e., ENSO) is crucial.

755    For the future, the Global Precipitation Measurement (GPM) mission will

756    significantly contribute to an improved record of intense precipitation, extending to a

757    more global domain, and allowing for a longer, enhanced climate record to be used. This

758    should allow a better specification of the intense precipitation relationships in the coming

759    years.

760    **Acknowledgments**

**References**

1. Adler, R. F., and Coauthors, 2003: The Version-2 Global Precipitation Climatology Project (GPCP) monthly precipitation analysis (1979–present). *J. Hydrometeor.*, **4**, 1147–1167, doi:10.1175/1525-7541(2003)004<1147:TVGPCP>2.0.CO;2.

2. Adler, R. F., G. Gu, J.-J. Wang, G. J. Huffman, S. Curtis, and D. Bolvin, 2008: Relationships between global precipitation and surface temperature on interannual and longer timescales (1979–2006). *J. Geophys. Res.*, **113**, D22104, doi:10.1029/2008JD010536.

3. Adler, R. F., J.-J. Wang, G. Gu, and G. J. Huffman, 2009: A ten-year tropical rainfall climatology based on a composite of TRMM products. *J. Meteor. Soc. Japan*, **87A**, 281–293, doi:10.2151/jmsj.87A.281.

4. Allan, R. P., and B. J. Soden, 2008: Atmospheric Warming and the Amplification of Precipitation Extremes. *Science,* **321,** 1481-1484, doi:10.1126/science.1160787.

5. Arkin, P. A., J. Turk, and E. Ebert, 2008: Pilot Evaluation of High Resolution Precipitation Products (PEHRPP): A contribution to GPM planning.

6. Benestad, R. E., D. Nychka, and L. O. Mearns, 2012: Spatially and temporally consistent prediction of heavy precipitation from mean values. *Nat. Clim. Change*, **2**, 544-547, doi:10.1038/NCLIMATE1497.

7. *Benestad, R. E., 2013: Association between trends in daily rainfall percentiles and the global mean temperature. J. Geophys. Res. Atmos.,* **118**, 10802–10810, doi:10.1002/jgrd.50814.*

790    8. Cavalcanti, I. F. A., 2012: Large scale and synoptic features associated with

791        extreme precipitation over South America: A review and case studies for the first

792        decade of the 21st century. *Atmos. Res.*, **118**, 27-40,

793        doi:10.1016/j.atmosres.2012.06.012.

794    9. Curtis, S., A. Salahuddin, R. F. Adler, G. J. Huffman, G. Gu, and Y. Hong, 2007:

795        Precipitation Extremes Estimated by GPCP and TRMM: ENSO Relationships. *J.*

796        *Hydrometeor.*, **8**, 678–689, doi:10.1175/JHM601.1.

797    10. Dai, A., I. Y. Fung, and A. D. Del Genio, 1997: Surface observed global land

798        precipitation variations during 1900–88. *J. Climate*, **10**, 2943–2962,

799        doi:10.1175/1520-0442(1997)010<2943:SOGLPV>2.0.CO;2.

800    11. Dai, A., 2011: Drought under global warming: A review. *Wiley Interdisciplinary*

801        *Reviews: Climate Change*, **2**, 45-65, doi:10.1002/wcc.81.

802    12. Easterling, D. R., J. L. Evans, P. Y. Groisman, T. R. Karl, K. E. Kunkel, and P.

803        Ambenje, 2000: Observed variability and trends in extreme climate events: A

804        brief review. *Bull. Amer. Meteor. Soc.*, **81**, 417–425, doi:10.1175/1520-

805        0477(2000)081<0417:OVATIE>2.3.CO;2.

806    13. Ebert, E. E., J. Janowiak, and C. Kidd, 2007: Comparison of near-real time

807        precipitation estimates from satellite observations and numerical models. *Bull.*

808        *Amer. Meteor. Soc.*, **88**, 47–64, doi:10.1175/BAMS-88-1-47.

809    14. Grimm, A. M., and R. G. Tedeschi, 2009: ENSO and extreme rainfall events in

810        South America. *J. Climate*, **22**, 1589-1609, doi:10.1175/2008JCLI2429.1.

811    15. Grimm, A. M., 2011: Interannual climate variability in South America: impacts

812        on seasonal precipitation, extreme events, and possible effects of climate change.

813       *Stoch. Environ. Res. Risk. Assess.*, **25**, 537-554, doi:10.1007/s00477-010-0420-1.

814       16. Grimm, A. M. and J. P. J. Saboia, 2015: Interdecadal Variability of the South

815       American Precipitation in the Monsoon Season. *J. Climate*, **28**, 755-775,

816       doi:10.1175/JCLI-D-14-00046.1.

817       17. Grimm, A. M., N. C. Laureanti, R. B. Rodakoviski, and C. B. Gama, 2016:

818       Interdecadal variability and extreme precipitation events in South America during

819       the monsoon season. *Climate Research*, **68**, 2-3, doi: 10.3354/cr01375.

820       18. Gu, G., R. F. Adler, G. J. Huffman, and S. Curtis, 2007: Tropical Rainfall

821       Variability on Interannual-to-Interdecadal and Longer Time Scales Derived from

822       the GPCP Monthly Product. *J. Climate*, **20**, 4033–4046, doi:10.1175/JCLI4227.1

823       19. Gustaffson, M., D. Rayner, and D. Chen, 2010: Extreme rainfall events in

824       southern Sweden: where does the moisture come from? *Tellus*, **62A**, 605-616,

825       doi:10.1111/j.1600-0870.2010.00456.x.

826       20. Held, I. M., and B. J. Soden, 2006: Robust responses of the hydrological cycle to

827       global warming. *J. Clim*ate, **19**, 5686–5699, doi:10.1175/JCLI3990.1.

828       21. Huffman, G. J., R. F. Adler, M. Morrissey, D. Bolvin, S. Curtis, R. Joyce, B.

829       McGavock, and J. Susskind, 2001: Global precipitation at one-degree daily

830       resolution from multi-satellite observations. *J. Hydrometeor.*, **2**, 36-50,

831       doi:10.1175/1525-7541(2001)002<0036:GPAODD>2.0.CO;2.

832       22. Huffman, G. J., and Coauthors, 2007: The TRMM Multisatellite Precipitation

833       Analysis (TMPA): Quasi-Global, Multiyear, Combined-Sensor Precipitation

834       Estimates at Fine Scales. *J. Hydrometeor.*, **8**, 38–55, doi:10.1175/JHM560.1.

835       23. Huffman, G. J., R. F. Adler, D. T. Bolvin, and G. Gu, 2009: Improving the global

836    precipitation record: GPCP Version 2.1. *Geophys. Res. Lett.*, **36**, L17808,

837    doi:10.1029/2009GL040000.

838  24. Huffman, G. J., R. F. Adler, D. T. Bolvin, and E. J. Nelkin, 2010: The TRMM

839    Multi-satellite Precipitation Analysis (TMPA). Chapter 1 in *Satellite Rainfall*

840    *Applications for Surface Hydrology*, F. Hossain and M. Gebremichael, Eds.,

841    Springer Verlag, ISBN: 978-90-481-2914-0, 3-22. [Available online at

842    ftp://precip.gsfc.nasa.gov/betsy/huffman/papers/TMPA_hydro_rev.pdf.]

843  25. Huffman, G. J., and D. T. Bolvin, 2012: TRMM and Other Data Precipitation

844    Data Set Documentation. Technical product document, 1-37. [Available online at

845    ftp://trmmopen.gsfc.nasa.gov/pub/merged/V7Documents/3B4XRT_doc_V7.pdf.]

846  26. IPCC, 2007. *Climate Change 2007: The Physical Science Basis*, S. Solomon, D.

847    Qin, M. Manning, Z. Chen, M. Marquis, K. B. Averyt, M. Tignor, H. L. Miller,

848    Eds., Contribution of Working Group I to the Fourth Assessment Report of the

849    Intergovernmental Panel on Climate Change, Cambridge University Press,

850    Cambridge, United Kingdom/New York, NY, USA, 996 pp.

851  27. Karl, T. R., N. Nicholls, and A. Ghazi, 1999: CLIVAR/GCOS/WMO workshop

852    on indices and indicators for climate extremes: Workshop summary. *Climatic*

853    *Change*, **42**, 3-7, doi:10.1023/A:1005491526870.

854  28. Kharin, V., F. W. Zwiers, X. Zhang, and G. C. Hergerl, 2007: Changes in

855    temperature and precipitation extremes in IPCC ensemble of coupled model

856    simulations. *J. Climate*, **20**, 1419–1444, doi:10.1175/JCLI4066.1.

857  29. Kirschbaum, D., R. Adler, D. Adler, C. Peters-Lidard, and G. Huffman, 2012:

858    Global Distribution of Extreme Precipitation and High-Impact Landslides in 2010

859     Relative to Previous Years. *J. Hydrometeor.*, **13**, 1536–1551, doi:10.1175/JHM-

860     D-12-02.1.

861     30. Lau, K.-M., and H.-T. Wu, 2011: Climatology and changes in tropical oceanic

862     rainfall characteristics inferred from Tropical Rainfall Measuring Mission

863     (TRMM) data (1998-2009). *J. Geophys. Res.*, **116**, D17111,

864     doi:10.1029/2011JD015827.

865     31. Lau, W. K.-M., H.-T. Wu, and K.-M. Kim, 2013: A canonical response of

866     precipitation characteristics to global warming from CMIP5 models. *Geophys.*

867     *Res. Lett.*, **40**, 3163–3169, doi:10.1002/grl.50420.

868     32. Liu, C. and R. P. Allan, 2012: Multi-satellite observed responses of precipitation

869     and its extremes to interannual climate variability. *J. Geophys. Res.,* **117,** D03101,

870     doi:10.1029/2011JD016568.

871     33. Min, S-K., X. Zhang, F. W. Zwiers, and G. C. Hegerl, 2011: Human contribution

872     to more-intense precipitation extremes. *Nature*, **470**, 378-381,

873     doi:10.1038/nature09763.

874     34. O'Gorman, P.A., 2012: Sensitivity of tropical precipitation extremes to climate

875     change. *Nature Geoscience*, **5**, 697-700, doi:10.1038/ngeo1568.

876     35. Peterson, T.C., C. Folland, G. Gruza, W. Hogg, A. Mokssit, and N. Plummer,

877     2001: Report on the Activities of the Working Group on Climate Change

878     Detection and Related Rapporteurs 1998-2001. *World Meteorological*

879     *Organization*, Rep. WCDMP-47, WMO-TD 1071, Geneva, Switzerland, 143 pp.

880     36. Sapiano, M. R. P., and P. A. Arkin, 2009: An inter-comparison and validation of

881     high resolution satellite precipitation estimates with three-hourly gauge data. *J.*

882     *Hydrometeor.,* **10**(1), 149-166, doi:10.1175/2008JHM1052.1.

883     37. Scheel, M. L. M., M. Rohrer, C. Huggel, D. S. Villar, E. Silvestre, and G. J.

884         Huffman, 2011: Evaluation of TRMM Multi-satellite Precipitation Analysis

885         (TMPA) performance in the Central Andes region and its dependency on spatial

886         and temporal resolution. *Hydrol. Earth Syst. Sci.*, **15**, 2649-2663,

887         doi:10.5194/hess-15-2649-2011.

888     38. Schneider, U., A. Becker, A. Meyer-Christoffer, M. Ziese and B. Rudolf, 2011:

889         Global Precipitation Analysis Products of the GPCC. Global Precipitation

890         Climatology Centre (GPCC), DWD, Internet Publikation, 13 pp.

891     39. Shiu, C.-J., S. C. Liu, C. Fu, A. Dai, and Y. Sun, 2012: How much do

892         precipitation extremes change in a warming climate? *Geophys. Res. Lett*., **39**,

893         L17707, doi:10.1029/2012GL052762.

894     40. Su, F., Y. Hong, and D. P. Lettenmaier, 2008: Evaluation of TRMM Multisatellite

895         Precipitation Analysis (TMPA) and its utility in hydrologic prediction in the La

896         Plata basin. *J. Hydrometeor*., **9**, 622–640, doi:10.1175/2007JHM944.1.

897     41. Tian, Y., and Coauthors, 2009: Component analysis of errors in satellite-based

898         precipitation estimates. *J. Geophys. Res*., **114**, D24101,

899         doi:10.1029/2009JD011949.

900     42. Trenberth, K. E., A. Dai, R. M. Rasmussen, and D. B. Parsons, 2003: The

901         changing character of precipitation. *Bull. Amer. Meteor. Soc*., **84**, 1205–1217,

902         doi:10.1175/BAMS-84-9-1205.

903   43. Wang, J.-J., R. F. Adler, G. J. Huffman, and D. Bolvin, 2014: An updated TRMM

904       composite climatology of tropical rainfall and its validation. *J. Climate*, **27**, 273-

905       284, doi:10.1175/JCLI-D-13-00331.1.

906   44. Wu H., R. F. Adler, Y. Hong, Y. Tian, and F. Policelli, 2012: Evaluation of

907       Global Flood Detection Using Satellite-Based Rainfall and a Hydrologic Model.

908       *J. Hydrometeor.*, **13**, 1268–1284, doi:10.1175/JHM-D-11-087.1.

**Figure Captions**

910 **Figure 1** (a) Annual, (b) January, and (c) July mean precipitation climatology ($R_{mean}$, mm

911 day$^{-1}$), derived from the TMPA 3B42 Version 7 data during 1998-2013.

912 **Figure 2** (a) Annual, (b) January, and (c) July mean climatological fraction of days with

913 precipitation >0 mm day$^{-1}$ ($F_0=R_{mean}/R_{cond}$), derived from the TMPA 3B42 Version 7 data

914 during 1998-2013.

915 **Figure 3** (a) Annual, (b) January, and (c) July mean climatological conditional

916 precipitation rate ($R_{cond}$, mm day$^{-1}$), derived from the TMPA 3B42 Version 7 data during

917 1998-2013.

918 **Figure 4** (a) Annual, (b) January, and (c) July mean 95$^{th}$ percentile daily precipitation

919 value ($R_{95p}$, mm day$^{-1}$), derived from the TMPA 3B42 Version 7 data during 1998-2013.

920 **Figure 5** (a) Annual, (b) January, and (c) July mean precipitation ≥95$^{th}$ percentile daily

921 precipitation ($R_{95}$, mm day$^{-1}$), derived from the TMPA 3B42 Version 7 data during 1998-

922 2013.

923 **Figure 6** Annual, January, and July mean precipitation (a)-(c) ≥25 mm day$^{-1}$ threshold

924 ($R_{25}$; mm day$^{-1}$) and (d)-(f) ≥50 mm day$^{-1}$ threshold ($R_{50}$; mm day$^{-1}$), derived from the

925 TMPA 3B42 Version 7 data during 1998-2013.

926 **Figure 7** (a) Annual, (b) January, and (c) July mean climatological fraction of daily

927 precipitation ≥25 mm day$^{-1}$ ($F_{25}=R_{25}/R_{mean}$), derived from the TMPA 3B42 Version 7

928 data during 1998-2013.

929 **Figure 8** Scatter plots of monthly climatology of mean precipitation ($R_{mean}$, mm day$^{-1}$)

930 and intense precipitation (a)-(b) ≥25 mm day$^{-1}$ ($R_{25}$, mm day$^{-1}$) and (c)-(d) ≥50 mm day$^{-1}$

931 ($R_{50}$, mm day$^{-1}$) over the TRMM domain (50°N-50°S), separately over land and ocean,

932    derived from the TMPA 3B42 Version 7 data during 1998-2013. The color bar indicates

933    the number of grid points with the attributed values in a logarithmic scale. Median (black

934    dashed line) is calculated for a distribution of all 12 months. Correlation coefficient and

935    RMS difference between intense rainfall ($R_{25}$ and $R_{50}$) and $R_{mean}$ are displayed.

936    Correlation values are significant at the 95% confidence level.

937    **Figure 9** Mean precipitation anomalies (mm day$^{-1}$) for 4 seasons (DJF, MAM, JJA, SON)

938    for (a)-(d) El Niño and (e)-(h) La Niña period, derived from the TMPA 3B42 Version 7

939    data during 1998-2013.

940    **Figure 10** Scatter plots of mean precipitation ($R_{mean}$, mm day$^{-1}$) and intense precipitation

941    $\geq$25 mm day$^{-1}$ ($R_{25}$, mm day$^{-1}$) anomalies for El Niño, La Niña and neutral period, over

942    the tropical domain (23.5°N-23.5°S), over (a)-(c) land and (d)-(f) ocean, derived from the

943    TMPA 3B42 Version 7 data during 1998-2013. The color bar indicates the number of

944    grid points with the attributed values in a logarithmic scale. Correlation coefficient

945    between $R_{25}$ and $R_{mean}$ is displayed. Correlation values are significant at the 95%

946    confidence level.

947    **Figure 11** (a) Time series of mean precipitation ($R_{mean}$, mm day$^{-1}$; blue line) and intense

948    precipitation $\geq$25 mm day$^{-1}$ ($R_{25}$, mm day$^{-1}$; black line) and $\geq$50 mm day$^{-1}$ ($R_{50}$, mm day$^{-1}$;

949    red line) anomalies, and (b) scatter plot of $R_{mean}$, $R_{25}$, and $R_{50}$, and Niño3.4 index

950    anomalies, averaged over a 5°x5° box over the West Pacific Ocean (6°S-1°S, 177°E-

951    182°E), derived from the TMPA 3B42 Version 7 precipitation data during 1998-2013.

952    Correlation coefficient and RMS difference between intense rainfall ($R_{25}$ and $R_{50}$) and

953    $R_{mean}$ are displayed in (a), and correlation coefficient between $R_{mean}$, $R_{25}$, and $R_{50}$ with
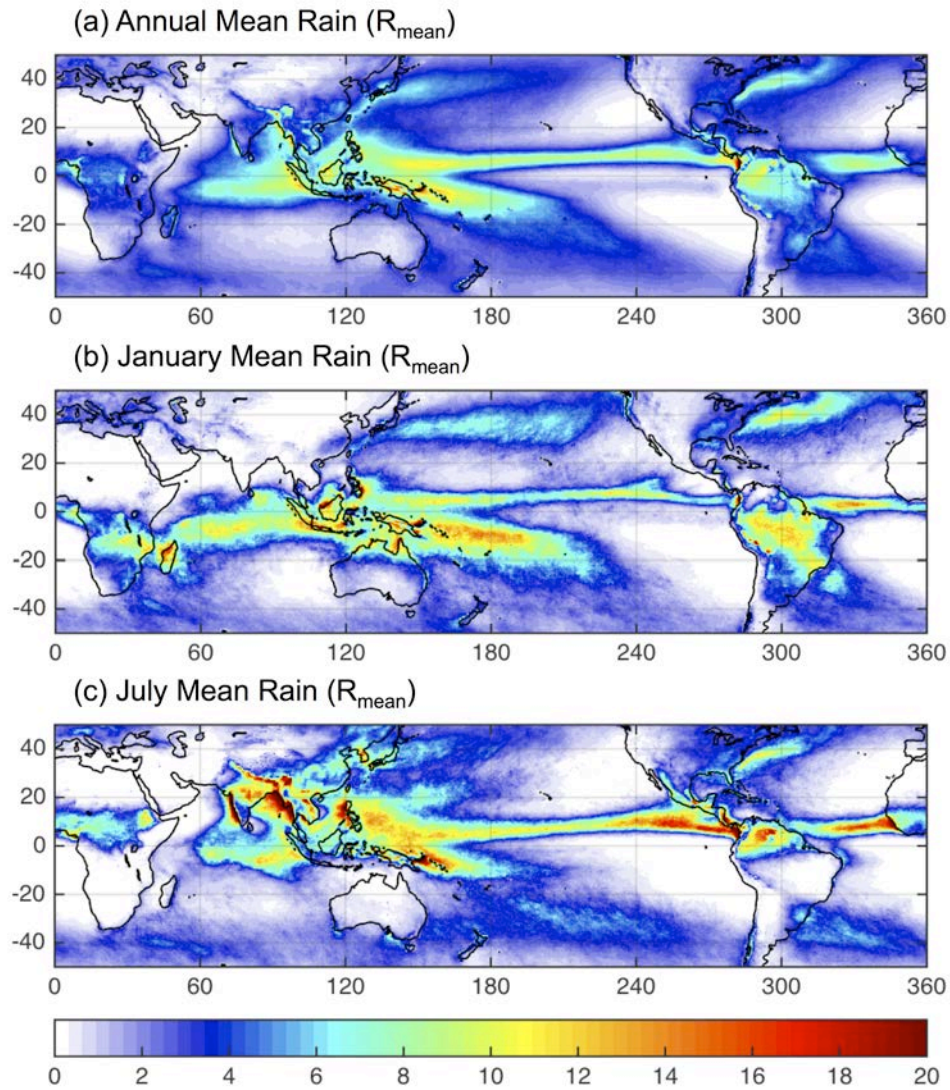
954 respect to the Niño3.4 index in (b). Correlation values are significant at the 95%

955 confidence level.

956 **Figure 12** Scatter plots of mean precipitation ($R_{mean}$; mm day$^{-1}$) and intense precipitation

957 $\geq 25$ mm day$^{-1}$ ($R_{25}$, mm day$^{-1}$; filled circles and black line) and $\geq 50$ mm day$^{-1}$ ($R_{50}$, mm

958 day$^{-1}$; empty circles and red line) anomalies, with corresponding linear fit for El Niño

959 (red), La Niña (blue) and neutral period (black), averaged over a 5°x5° box over: (a) the

960 West Pacific Ocean, (b) Philippines, (c) La Plata basin, and (d) Amazonia, derived from

961 the TMPA 3B42 Version 7 data during 1998-2013. 5°x5° boxes are chosen denoting two

962 largest maximums and minimums observed in global anomalies. Correlation coefficient

963 and RMS difference between intense rainfall ($R_{25}$ and $R_{50}$) and $R_{mean}$ are displayed.

964 Correlation values are significant at the 95% confidence level.

965 **Table Captions**

966 **Table 1** Definitions and units for monthly parameters of mean and intense precipitation**.**

968 **Table 1** Definitions and units for monthly parameters of mean and intense precipitation.

| Definition | Parameter | Unit |
|---|---|---|
| Daily precipitation | $R$ | mm day$^{-1}$ |
| **MEAN PRECIPITATION:** | | |
| Monthly mean precipitation (total amount of precipitation in a month/total days in a month) | $R_{mean}$ | mm day$^{-1}$ |
| Mean conditional precipitation rate (mean precipitation rate for days with R >0 mm day$^{-1}$) | $R_{cond}$ | mm day$^{-1}$ |
| Fraction of days in a month with R >0 mm day$^{-1}$ ($R_{mean}/R_{cond}$) | $F_0$ | |
| **INTENSE PRECIPITATION:** | | |
| 95$^{th}$ percentile of daily precipitation in a month | $R_{95p}$ | mm day$^{-1}$ |
| Monthly mean precipitation with R $\geq$95$^{th}$ percentile (Total R $\geq R_{95p}$ in a month/total days in a month) | $R_{95}$ | mm day$^{-1}$ |
| Fraction of daily precipitation with R $\geq$95$^{th}$ percentile ($R_{95}/R_{mean}$) | $F_{95}$ | |
| Monthly mean precipitation with R $\geq$25 and 50 mm day$^{-1}$ (Total R $\geq$25 and 50 mm day$^{-1}$ in a month/total days in a month) | $R_{25}, R_{50}$ | mm day$^{-1}$ |
| Number of days within a month with R $\geq$25, 50 and 75 mm day$^{-1}$ threshold | $N_{25}, N_{50}, N_{75}$ | day |
| Fraction of daily precipitation with R $\geq$25 and 50 mm day$^{-1}$ ($R_{25}/R_{mean}$ and $R_{50}/R_{mean}$) | $F_{25}, F_{50}$ | |

**Figures**

(a) Annual Mean Rain ($R_{mean}$)

(b) January Mean Rain ($R_{mean}$)

(c) July Mean Rain ($R_{mean}$)

**FIG. 1.** (a) Annual, (b) January, and (c) July mean precipitation climatology ($R_{mean}$, mm day$^{-1}$), derived from the TMPA 3B42 Version 7 data during 1998-2013.
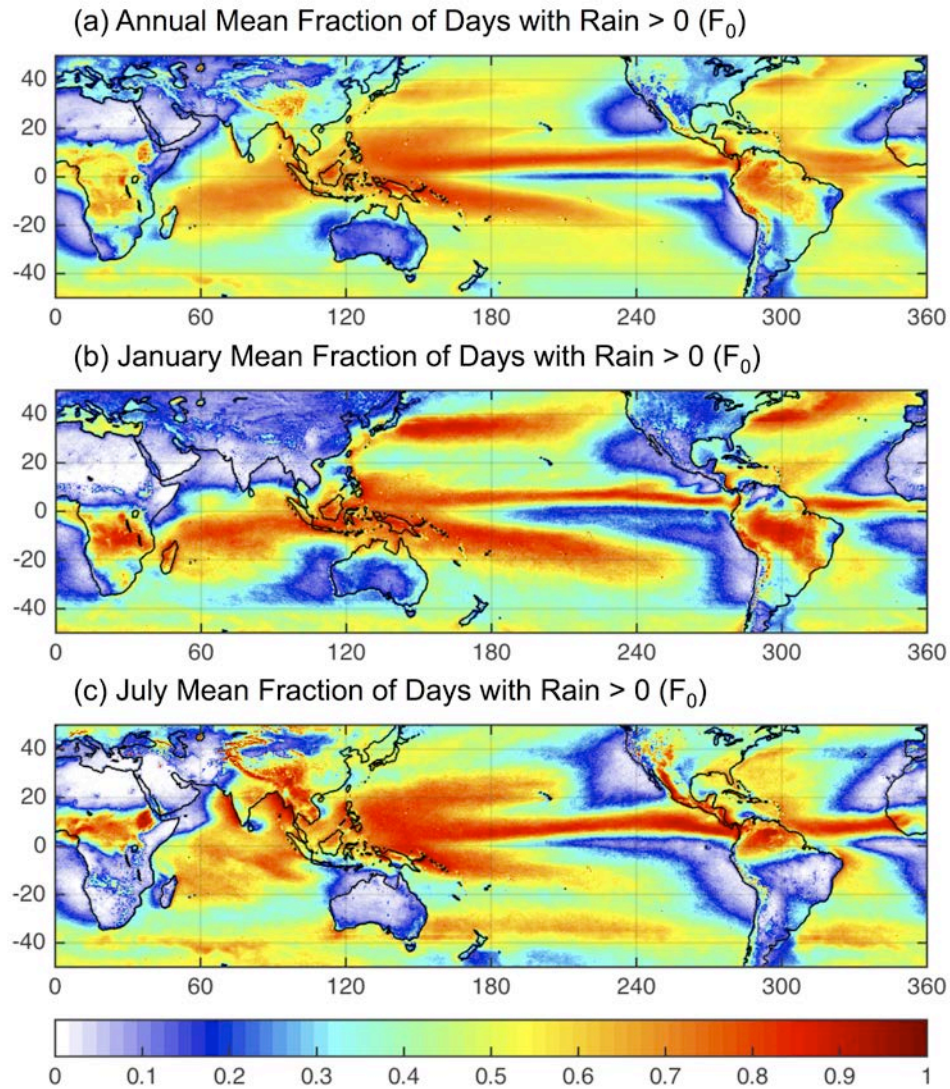
**FIG. 2.** (a) Annual, (b) January, and (c) July mean climatological fraction of days with precipitation >0 mm day$^{-1}$ ($F_0 = R_{mean}/R_{cond}$), derived from the TMPA 3B42 Version 7 data during 1998-2013.
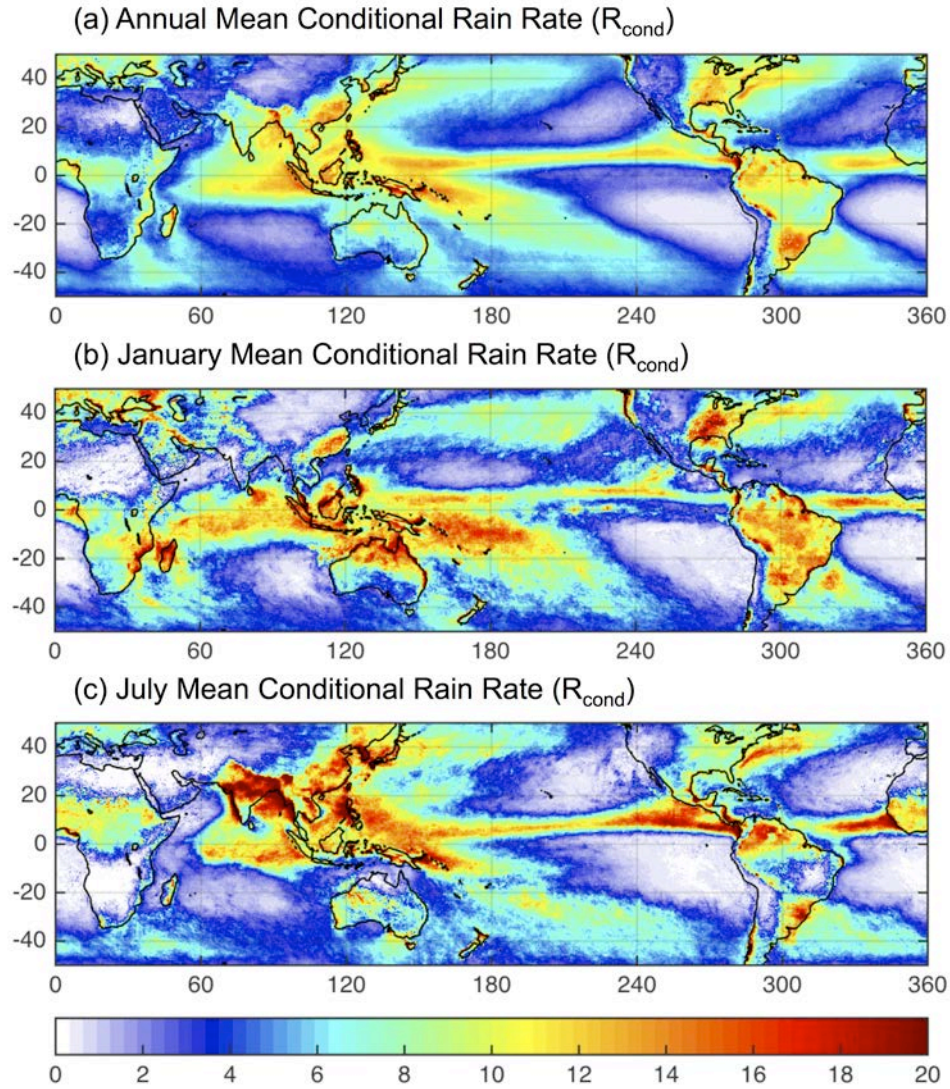
**FIG. 3.** (a) Annual, (b) January, and (c) July mean climatological conditional precipitation rate ($R_{cond}$, mm day$^{-1}$), derived from the TMPA 3B42 Version 7 data during 1998-2013.

## (a) Annual Mean 95th Percentile (R95p)

## (b) January Mean 95th Percentile (R95p)

## (c) July Mean 95th Percentile (R95p)
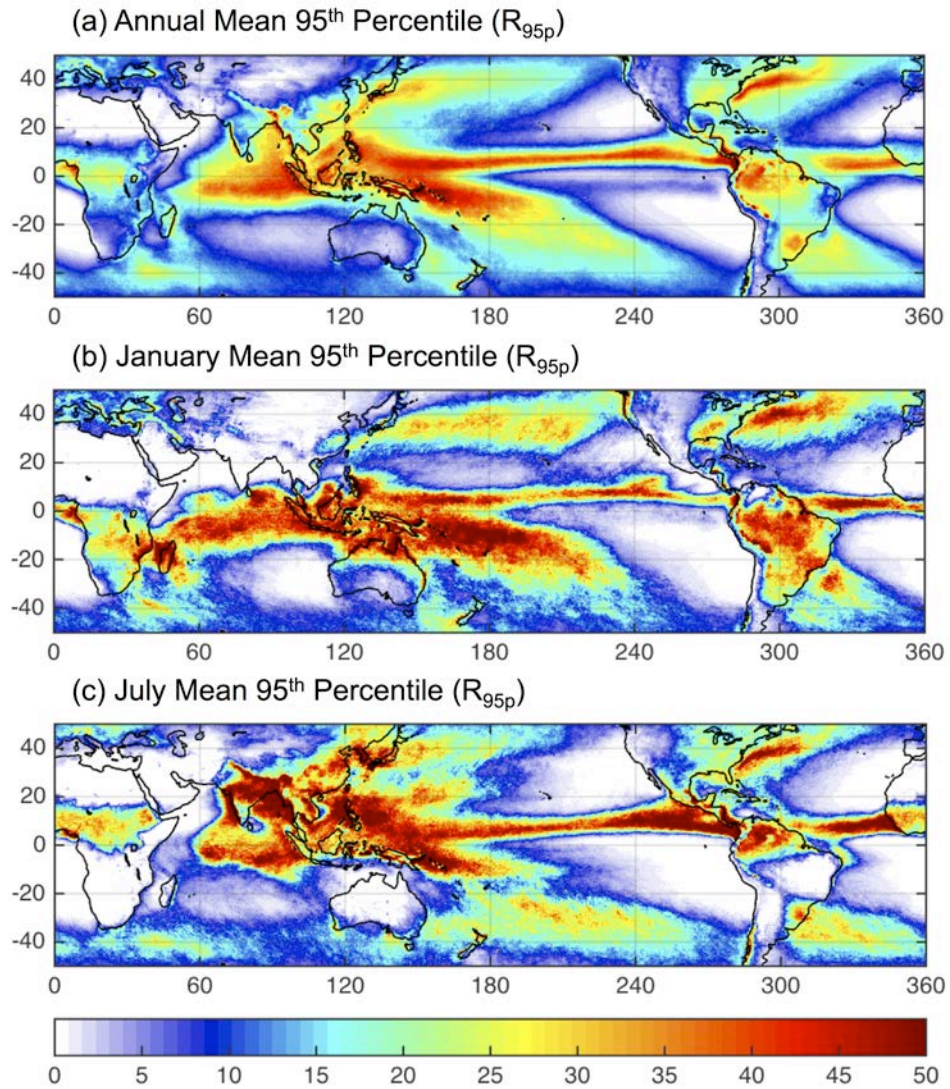
FIG. 4. (a) Annual, (b) January, and (c) July mean 95th percentile daily precipitation value ($R_{95p}$, mm day$^{-1}$), derived from the TMPA 3B42 Version 7 data during 1998-2013.

981
982
983

(a) Annual Mean Rain ≥ 95th Percentile ($R_{95}$)

(b) January Mean Rain ≥ 95th Percentile ($R_{95}$)
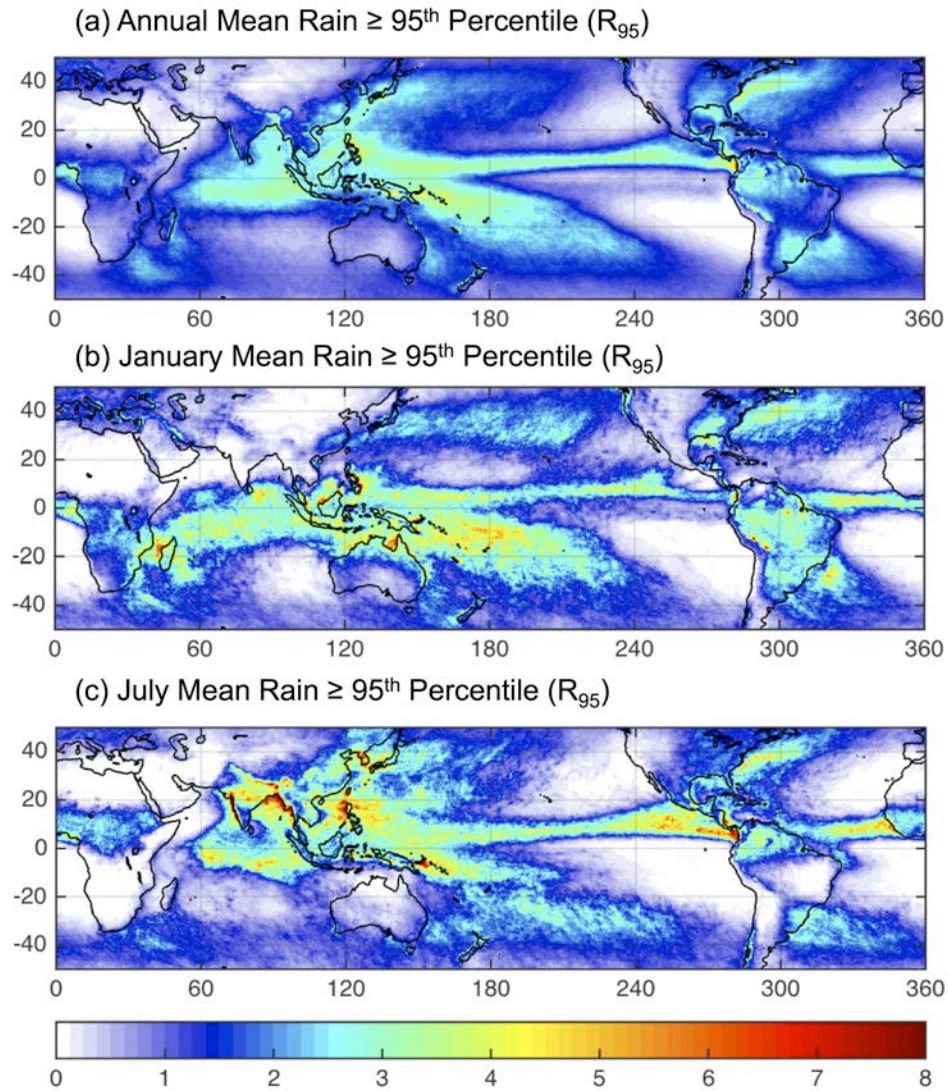
(c) July Mean Rain ≥ 95th Percentile ($R_{95}$)

**FIG. 5.** (a) Annual, (b) January, and (c) July mean precipitation ≥95th percentile daily precipitation ($R_{95}$, mm day$^{-1}$), derived from the TMPA 3B42 Version 7 data during 1998-2013.
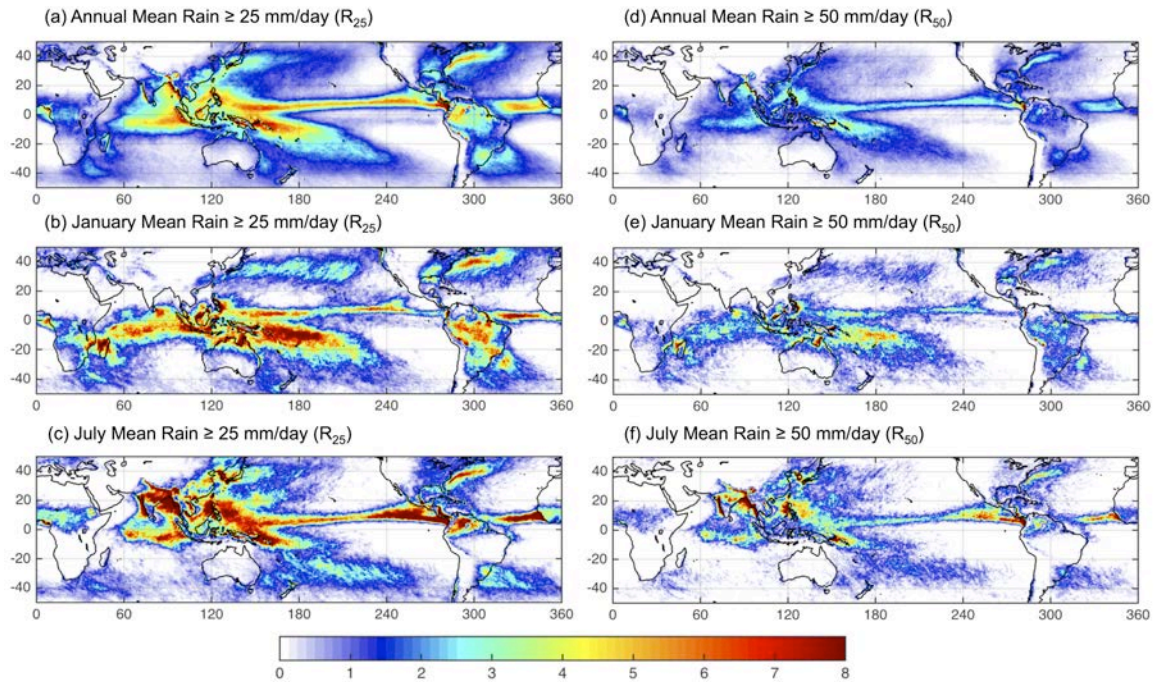
**FIG. 6.** Annual, January, and July mean precipitation (a)-(c) $\geq 25$ mm day$^{-1}$ threshold ($R_{25}$; mm day$^{-1}$) and (d)-(f) $\geq 50$ mm day$^{-1}$ threshold ($R_{50}$; mm day$^{-1}$), derived from the TMPA 3B42 Version 7 data during 1998-2013.
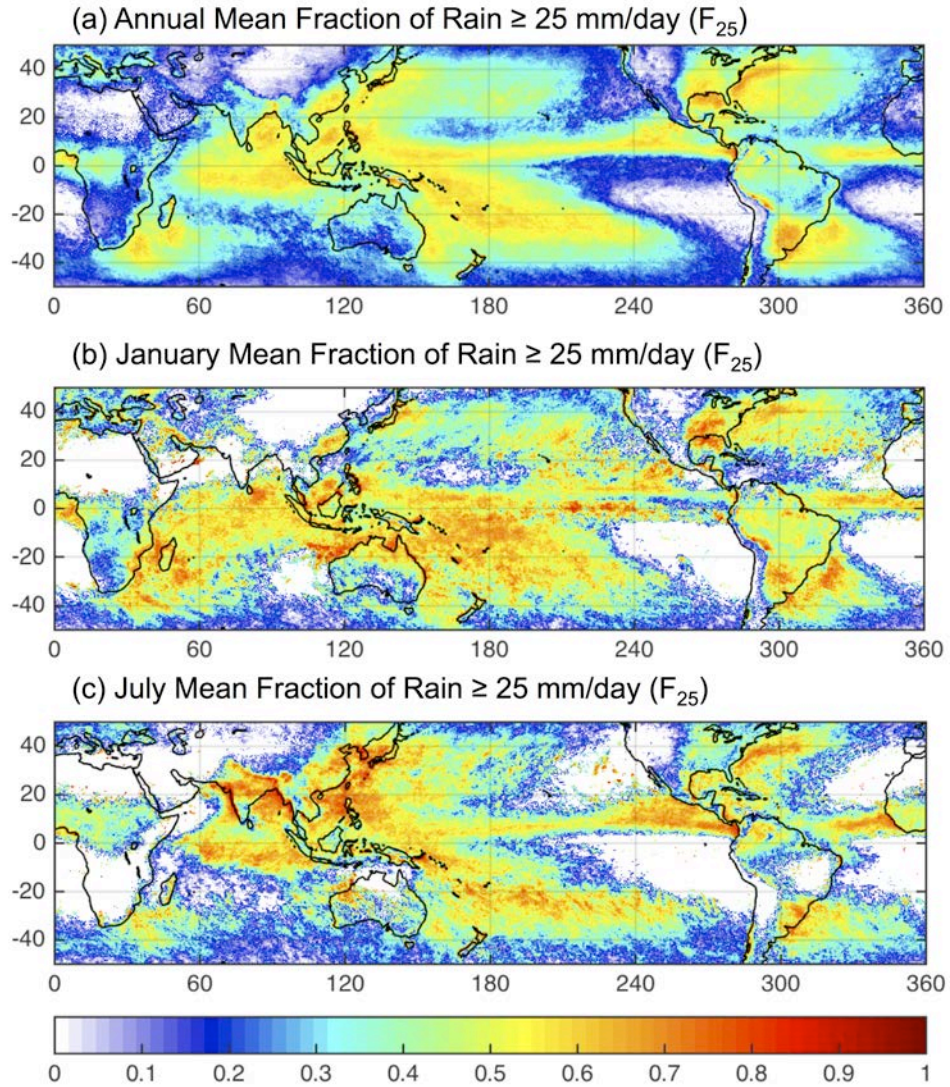
**FIG. 7.** (a) Annual, (b) January, and (c) July mean climatological fraction of daily precipitation $\geq 25$ mm day$^{-1}$ ($F_{25}=R_{25}/R_{mean}$), derived from the TMPA 3B42 Version 7 data during 1998-2013.
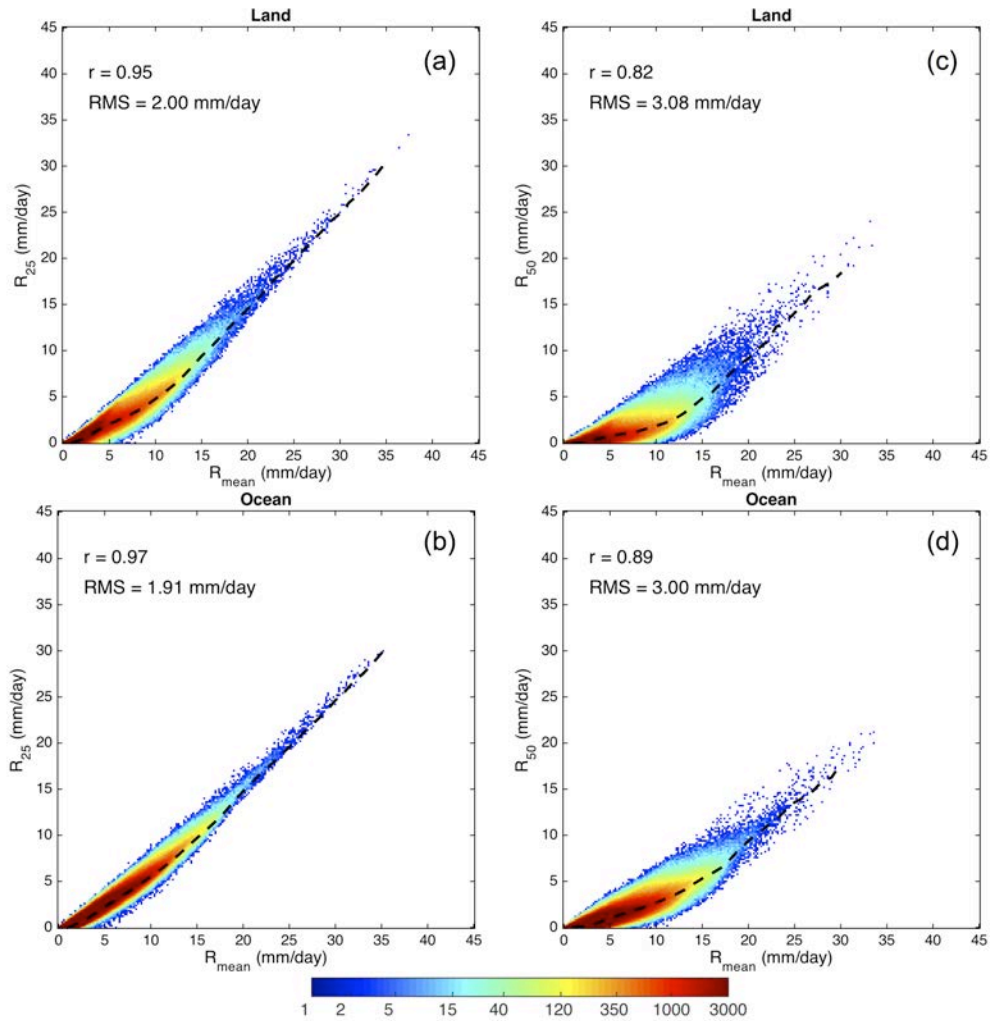
**FIG. 8.** Scatter plots of monthly climatology of mean precipitation ($R_{mean}$, mm day$^{-1}$) and intense precipitation (a)-(b) ≥25 mm day$^{-1}$ ($R_{25}$, mm day$^{-1}$) and (c)-(d) ≥50 mm day$^{-1}$ ($R_{50}$, mm day$^{-1}$) over the TRMM domain (50°N-50°S), separately over land and ocean, derived from the TMPA 3B42 Version 7 data during 1998-2013. The color bar indicates the number of grid points with the attributed values in a logarithmic scale. Median (black dashed line) is calculated for a distribution of all 12 months. Correlation coefficient and RMS difference between intense rainfall ($R_{25}$ and $R_{50}$) and $R_{mean}$ are displayed. Correlation values are significant at the 95% confidence level.
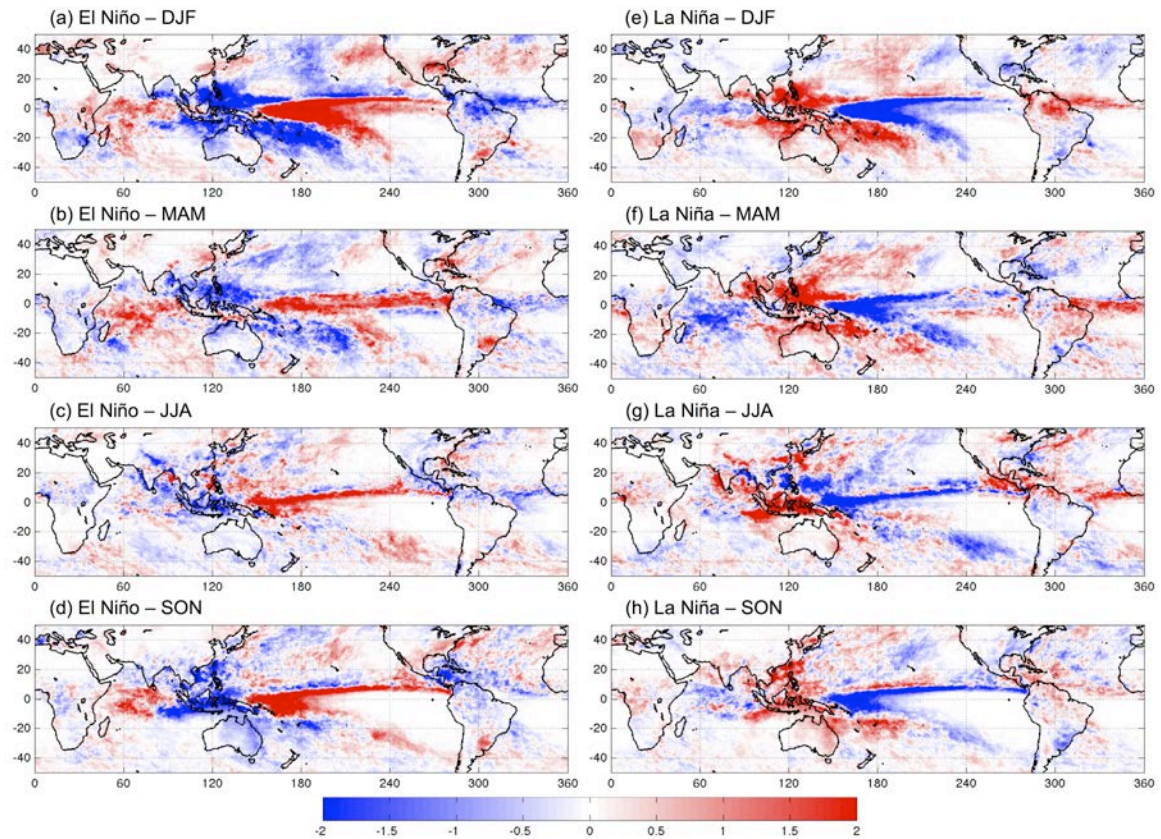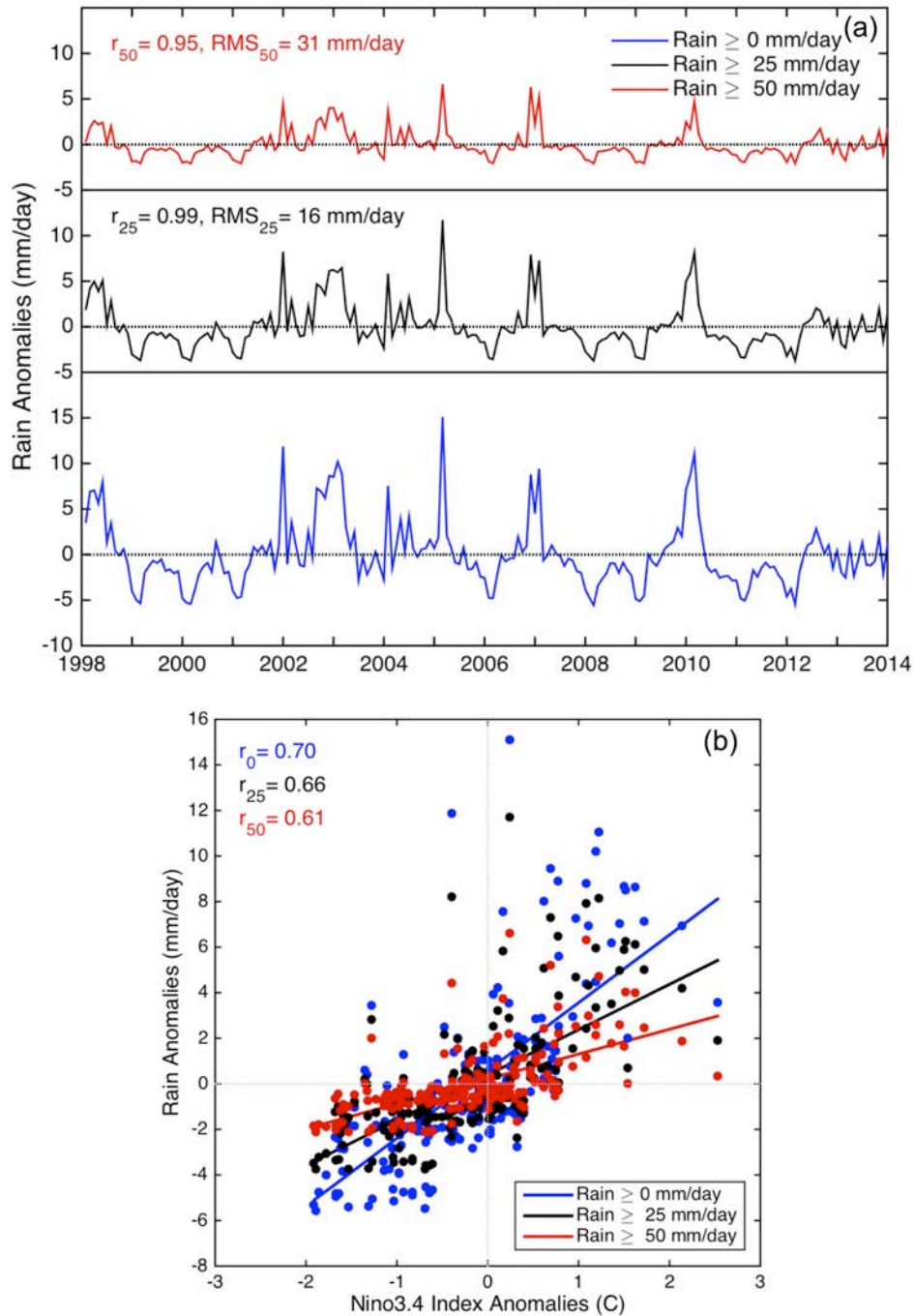
1005

**FIG. 9.** Mean precipitation anomalies (mm day$^{-1}$) for 4 seasons (DJF, MAM, JJA, SON)
for (a)-(d) El Niño and (e)-(h) La Niña period, derived from the TMPA 3B42 Version 7
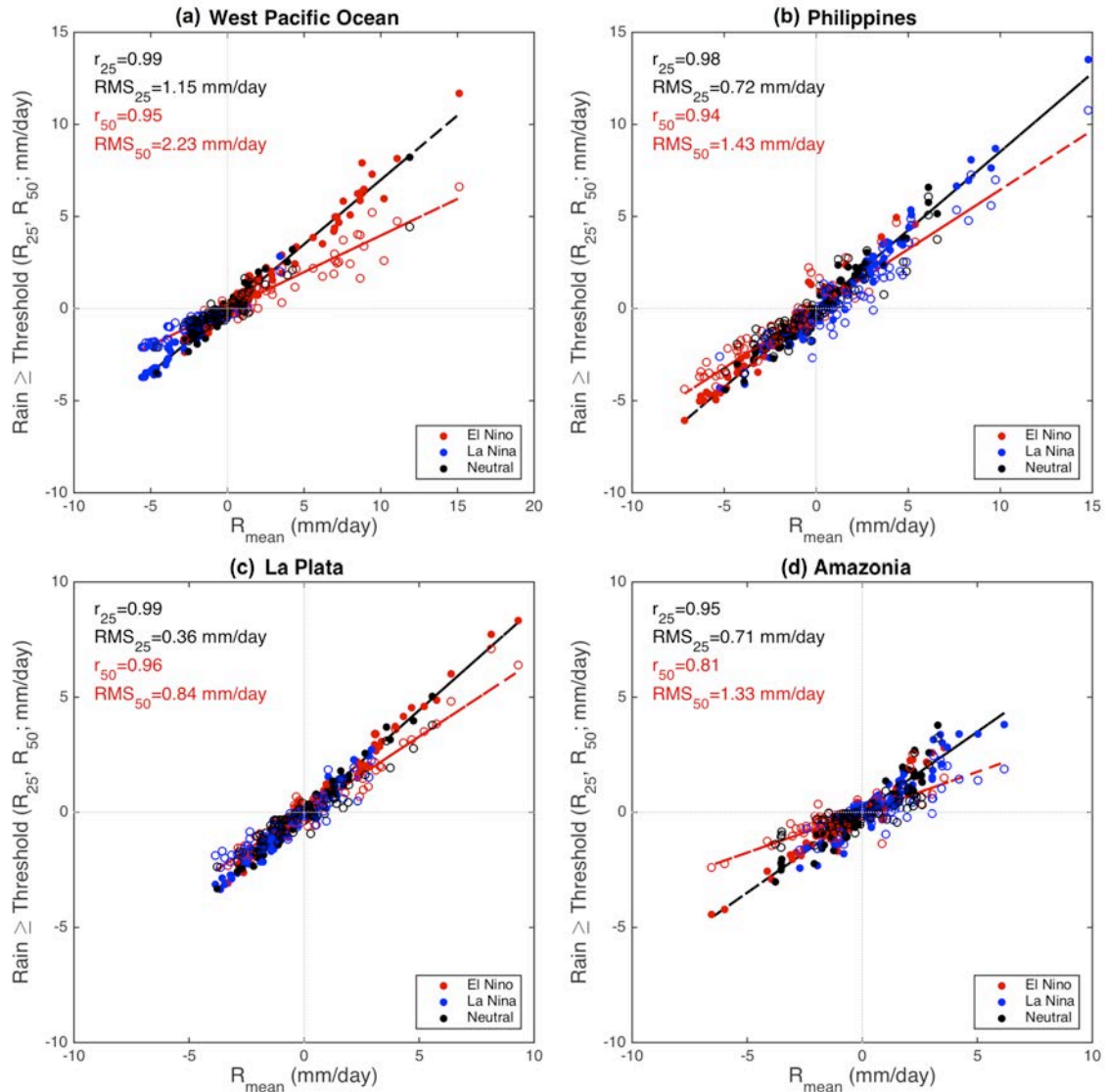data during 1998-2013.

**FIG. 10.** Scatter plots of mean precipitation ($R_{mean}$, mm day$^{-1}$) and intense precipitation $\geq 25$ mm day$^{-1}$ ($R_{25}$, mm day$^{-1}$) anomalies for El Niño, La Niña and neutral period, over the tropical domain (23.5°N-23.5°S), over (a)-(c) land and (d)-(f) ocean, derived from the TMPA 3B42 Version 7 data during 1998-2013. The color bar indicates the number of grid points with the attributed values in a logarithmic scale. Correlation coefficient between $R_{25}$ and $R_{mean}$ is displayed. Correlation values are significant at the 95% confidence level.

1017

**FIG. 11.** (a) Time series of mean precipitation ($R_{mean}$, mm day$^{-1}$; blue line) and intense precipitation ≥25 mm day$^{-1}$ ($R_{25}$, mm day$^{-1}$; black line) and ≥50 mm day$^{-1}$ ($R_{50}$, mm day$^{-1}$; red line) anomalies, and (b) scatter plot of $R_{mean}$, $R_{25}$, and $R_{50}$, and Niño3.4 index anomalies, averaged over a 5°x5° box over the West Pacific Ocean (6°S-1°S, 177°E-182°E), derived from the TMPA 3B42 Version 7 precipitation data during 1998-2013. Correlation coefficient and RMS difference between intense rainfall ($R_{25}$ and $R_{50}$) and $R_{mean}$ are displayed in (a), and correlation coefficient between $R_{mean}$, $R_{25}$, and $R_{50}$ with respect to the Niño3.4 index in (b). Correlation values are significant at the 95% confidence level.

1027
**FIG. 12.** Scatter plots of mean precipitation ($R_{mean}$; mm day$^{-1}$) and intense precipitation $\geq 25$ mm day$^{-1}$ ($R_{25}$, mm day$^{-1}$; filled circles and black line) and $\geq 50$ mm day$^{-1}$ ($R_{50}$, mm day$^{-1}$; empty circles and red line) anomalies, with corresponding linear fit for El Niño (red), La Niña (blue) and neutral period (black), averaged over a 5°x5° box over: (a) the West Pacific Ocean, (b) Philippines, (c) La Plata basin, and (d) Amazonia, derived from the TMPA 3B42 Version 7 data during 1998-2013. 5°x5° boxes are chosen denoting two largest maximums and minimums observed in global anomalies. Correlation coefficient and RMS difference between intense rainfall ($R_{25}$ and $R_{50}$) and $R_{mean}$ are displayed. Correlation values are significant at the 95% confidence level.